Hiroshima University

Master's Thesis

Performance Evaluation System of AC-coupled Low Gain Avalanche Detector (AC-LGAD) for Precise 4D Tracking at the EIC-ePIC Experiment

Author:
Kanato MATSUTANI

Supervisor:
Prof. Kenta SHIGAKI

Examiners:
Associate Prof. Makoto UEMURA
Assistant Prof. Masataka IINUMA

A thesis submitted in fulfillment of the requirements
for the degree of Master of Science
in the

Quark Physics Laboratory
Graduate School of Advanced Science and Engineering

February 20, 2026

Abstract

The Electron-Ion Collider (EIC) is a future collider experiment designed to unravel the remaining mysteries of the proton, such as its mass origin and spin structure. In the ePIC experiment at the EIC, the Barrel Time-of-Flight (BTOF) detector plays a crucial role in particle identification, requiring an excellent time resolution of approximately 35 ps and a spatial resolution of $O(10)$ μm. The AC-coupled Low Gain Avalanche Detector (AC-LGAD) is the baseline sensor technology selected to meet these stringent requirements due to its internal gain and charge sharing capabilities.

The primary objective of this thesis is to establish a comprehensive performance evaluation environment for AC-LGAD sensors at Hiroshima University and to characterize the fundamental properties of a prototype strip-type AC-LGAD. An experimental setup was constructed using a ^{90}Sr beta source, a constant-temperature bath for precise temperature control, and a high-speed readout system.

We evaluated the time resolution, charge sharing characteristics for position estimation, and the temperature dependence of the Current-Voltage (I-V) characteristics. The measurements confirmed that the AC-LGAD sensor exhibits signal induction on multiple electrodes, which enables precise hit position reconstruction. A time resolution of approximately 60 ps was achieved in the initial setup using the beta source. Furthermore, the correlation between temperature and the optimal bias voltage was systematically measured, providing essential feedback for the detector operation in the actual ePIC experiment.

These results demonstrate the successful establishment of the evaluation framework and contribute to the development of the BTOF detector for the EIC-ePIC experiment.

Acknowledgements

I would like to express my deepest gratitude to all those who have supported and encouraged me throughout my Master's studies.

First and foremost, I wish to express my sincere gratitude to my supervisor, **Professor Kenta Shigaki**. He introduced me to the fascinating world of Electron-Ion Collider (EIC) physics in my third year of undergraduate studies and provided me with numerous opportunities to attend conferences both in Japan and abroad. I am especially grateful for his kind support and guidance during the times when I struggled with my motivation; his encouragement allowed me to persevere and complete this research. The experiences I gained under his supervision will undoubtedly be the foundation for my future doctoral studies.

I would like to extend my heartfelt thanks to **Assistant Professor Satoshi Yano**. As the person in charge of BTOF for the ePIC Japan group, he provided invaluable advice on everything from experimental setups to data analysis. I cannot thank him enough for his constant availability for discussion and for his efficiency in arranging the necessary equipment for my research.

I am also grateful to the faculty members of the laboratory for their insightful comments. **Associate Professor Yorito Yamaguchi** provided valuable perspectives from the standpoint of future semiconductor detector upgrades for the ALICE experiment. **Associate Professor Kensuke Homma** helped me clarify the fundamental theories and underlying motivations of my research through his thought-provoking questions. **Assistant Professor Takahiro Miyoshi** always ensured I focused on the essential aspects of my presentations to improve their quality; I was also personally touched by his warm concern when he asked if I enjoyed my research trips.

Special thanks are due to the professors and researchers involved in the EIC project. Their advice during weekly progress reports and support during my stay in the U.S. were indispensable. In particular, I would like to thank **Dr. Koji Nakamura** from KEK. When I was a complete novice regarding AC-LGAD, he allowed me to participate in characterization tests at the KEK laboratory. This experience was a major stepping stone for the start of my research.

To my fellow M2 students, thank you for making my daily life so fulfilling. Whether we were traveling, sharing drinks, or simply chatting, you were the best companions I could ask for. I have lost count of how many times we visited our favorite *motsunabe* restaurant for parties. Although we are now heading toward different career paths, I wish you all the very best. I also thank my seniors for their career advice and my juniors for creating such a friendly and welcoming atmosphere in the lab.

Finally, I would like to thank my family. Despite being stationed in China for work during my Master's course, you checked in on me regularly. I truly enjoyed the photos of beautiful landscapes you sent from China, and your support was a great help during my long-term stays abroad. Thank you for everything.

Contents

List of Figures

Chapter 1

Introduction

1.1 Physics Motivation

1.1.1 Standard Model and Quantum Chromodynamics

The Standard Model of particle physics has been remarkably successful in describing the fundamental constituents of matter and their interactions. Within this framework, protons and neutrons, collectively known as nucleons, are composite particles formed by quarks and gluons (Figure 1.1). Their dynamics are governed by Quantum Chromodynamics (QCD), the theory of the strong interaction. Unlike Quantum Electrodynamics (QED), QCD exhibits two unique properties: confinement and asymptotic freedom [6, 7]. Confinement implies that color-charged particles (quarks and gluons) cannot be isolated, while asymptotic freedom dictates that the interaction strength decreases at short distances (high energy scales), allowing for perturbative calculations.

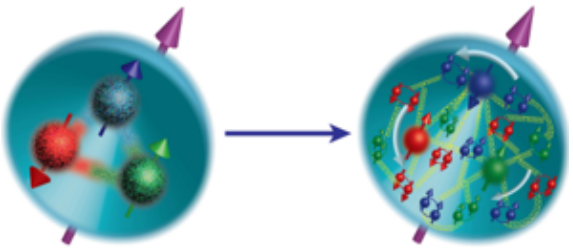

Figure 1.1: A conceptual illustration of the proton structure, composed of valence quarks, sea quarks, and gluons governed by QCD dynamics. [1]

Despite the success of the Standard Model, fundamental questions regarding the nucleon structure remain unanswered. One of the most profound puzzles is the origin of the nucleon mass. The discovery of the Higgs boson explained the origin of the current quark masses (u and d quarks), but these account for only about 1% of the proton's mass (~ 938 MeV/c^2), as illustrated in Figure 1.2. The remaining 99% is believed to emerge dynamically from the strong interaction, specifically related to the spontaneous breaking of chiral symmetry and the trace anomaly of the energy-momentum tensor in QCD [8,9]. Understanding how the mass of the visible universe emerges from massless gluons and nearly massless quarks is a central goal of modern nuclear physics.

Figure 1.2: Illustration of the proton mass puzzle. The Higgs mechanism accounts for only a small fraction of the proton mass, with the majority emerging from the dynamics of quarks and gluons. [1]

1.1.2 Electron Scattering and Deep Inelastic Scattering

To probe the internal structure of the nucleon, lepton-nucleon scattering has served as a powerful microscope. The most fundamental process is Deep Inelastic Scattering (DIS), where a high-energy electron scatters off a nucleon by exchanging a virtual photon with four-momentum transfer squared Q^2 (Figure 1.3). By measuring the scattered electron, one can determine the parton distribution functions (PDFs), which describe the probability of finding a quark or gluon with a longitudinal momentum fraction x.

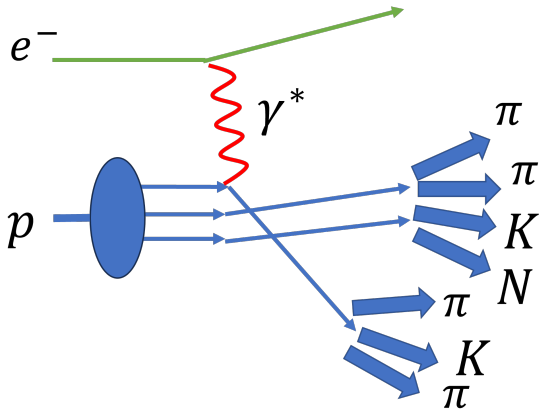

Figure 1.3: Feynman diagram of Deep Inelastic Scattering (DIS), where an electron e scatters off a proton p via the exchange of a virtual photon γ^*, probing the internal quark structure.

While inclusive DIS ($e + p \rightarrow e' + X$) provides information on the 1-dimensional structure of the nucleon, it integrates over the transverse degrees of freedom. To access the 3-dimensional structure and unravel the spin and mass mechanisms, Semi-Inclusive Deep Inelastic Scattering (SIDIS) is essential. In SIDIS ($e+p \rightarrow e'+h+X$), a hadron h is detected in coincidence with the scattered electron. The properties of the detected hadron carry information about the flavor and transverse motion of the struck quark, enabling access to Transverse Momentum Dependent parton distributions (TMDs) and Generalized Parton Distributions (GPDs).

1.2 The Electron-Ion Collider (EIC) Project

To address the fundamental questions of nucleon structure and QCD dynamics, the Electron-Ion Collider (EIC) is currently being realized at Brookhaven National Laboratory (BNL) on Long Island, New York (Figure 1.4a). The EIC is a next-generation high-luminosity collider designed to collide polarized electrons with polarized protons and light ions, as well as heavy nuclei. It will utilize the existing Relativistic Heavy Ion Collider (RHIC) tunnel, adding a new electron storage ring to collide with the hadron beams (Figure 1.4b and 1.4c). It functions as a precision "femto-scope," probing the internal landscape of nucleons with unprecedented resolution [10].

(a) Aerial view of BNL.

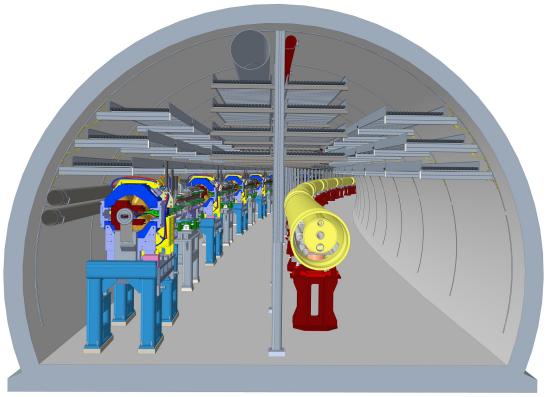

(b) Artist's impression of the EIC tunnel.

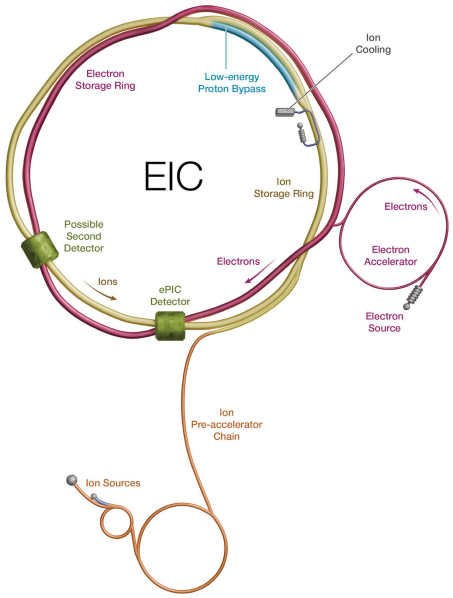

(c) Schematic layout of the EIC.

Figure 1.4: Overview of the Electron-Ion Collider (EIC) project at Brookhaven National Laboratory. (a) Aerial view of the BNL site showing the RHIC ring. (b) Schematic layout of the EIC illustrating the electron and hadron storage rings and the interaction regions. (c) A rendering of the accelerator tunnel. [1]

According to the latest design status reported in January 2026, the machine parameters are being finalized to meet the scientific mission [11]:

- **High Luminosity:** The EIC targets a peak luminosity of 10^{33}–10^{34} $\text{cm}^{-2}\text{s}^{-1}$, essential for multi-dimensional 3D nucleon imaging.
- **Variable Center-of-Mass Energy:** The center-of-mass energy ($\sqrt{s}$) ranges from 20 to 140 GeV, covering a wide kinematic plane.
- **Highly Polarized Beams:** Spin-polarized beams for both electrons and hadrons (approx. 70% polarization) are a unique feature for spin physics [11].
- **Diverse Ion Species:** The collider accommodates ion species from protons to heavy nuclei (Au, U) to study gluon saturation [12].

The project is progressing according to the schedule outlined by the U.S. Department of Energy (DOE), with the aim of commencing operations in the early 2030s (Figure 1.5).

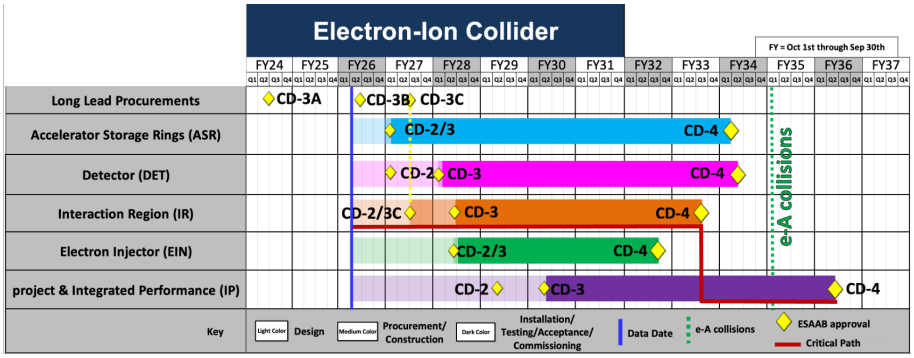

Figure 1.5: Overview of the EIC project schedule, indicating key milestones such as CD (Critical Decision) approvals and the start of operations. [2]

1.3 EIC Physics Goals and Experimental Approaches

With the unique capabilities described above, the EIC will explore four major frontiers: the origin of nucleon mass, the proton spin puzzle, 3D imaging of the nucleon, and gluon saturation. To achieve these goals, specific collision processes and experimental methodologies have been identified.

1.3.1 Origin of Nucleon Mass and Hadronization

The mass of the proton is generated largely by the dynamics of gluons, related to the QCD trace anomaly.

- **Process:** The threshold production of vector mesons, such as J/ψ and Υ, in electron-proton collisions ($e + p \rightarrow e' + V + p$).
- **Experimental Approach:** The cross-section of heavy quarkonium production near the threshold is sensitive to the trace of the energy-momentum tensor of QCD.Measuring this process requires precise detection of the scattered electron and the decay products of the vector meson [13, 14].
- **Hadronization:** Additionally, by using heavy nuclei (e.g., C, Cu, Au) as targets ($e + A$), the EIC will study the hadronization process. The nuclear medium acts as a detector of known size, allowing the measurement of energy loss and the nuclear modification factor (R_{eA}) to determine the time scale of color neutralization.

1.3.2 Proton Spin and Flavor Structure

The decomposition of the proton spin (1/2) into contributions from quarks, gluons, and their orbital angular momenta is a central theme, often referred to as the "proton spin puzzle" (Figure 1.6).

Figure 1.6: Conceptual representation of the proton spin puzzle, illustrating the incomplete understanding of how quark spins, gluon spins, and orbital angular momenta contribute to the total proton spin. [1]

- **Process:** Polarized Semi-Inclusive Deep Inelastic Scattering (SIDIS), $e + p^{\uparrow} \rightarrow e' + h + X$, where polarized electron beams collide with transversely polarized protons (Figure 1.7).
- **Experimental Approach:** The key observable is the single spin asymmetry of the produced hadrons. This asymmetry arises from phenomena such as the Sivers effect (correlation between nucleon spin and quark transverse momentum) [15] and the Collins effect (correlation between quark spin and hadron fragmentation) [16].
- **Requirement for PID:** Crucially, to separate the contributions of up, down, and strange quarks (flavor decomposition), the detector must distinguish the flavor of the produced hadron h (i.e., identifying $\pi^{\pm}$, $K^{\pm}$, p). This necessitates excellent Particle Identification (PID) capabilities, utilizing technologies like RICH, DIRC, and Time-of-Flight (TOF) systems.

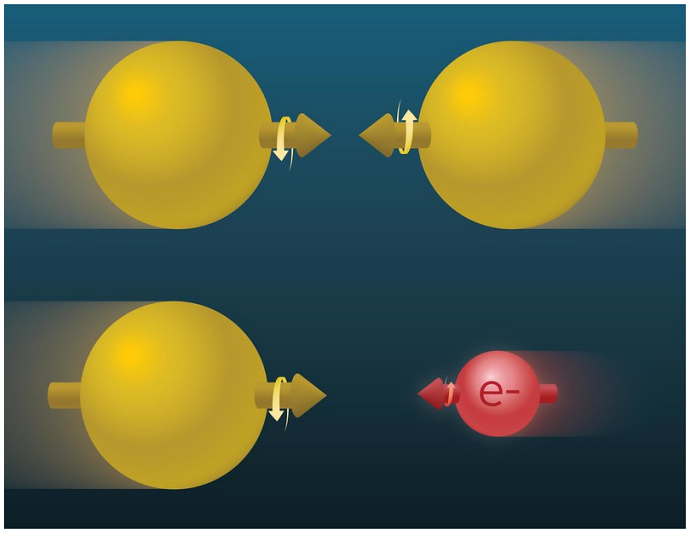

Figure 1.7: Illustration of collisions between polarized electron and polarized proton beams at the EIC, which are essential for probing the spin structure of the nucleon. [1]

1.3.3 3D Imaging of the Nucleon

The EIC aims to map the internal landscape of the nucleon in terms of position and momentum, analogous to medical tomography.

- **GPDs (Position):** Deeply Virtual Compton Scattering (DVCS), $e + p \to e' + \gamma + p'$, probes Generalized Parton Distributions (GPDs) [17]. This process requires the detection of the emitted photon and, crucially, the recoiling proton p' which stays intact. Far-forward detectors like Roman Pots are essential to capture these protons scattered at very small angles.
- **TMDs (Momentum):** As mentioned in the spin section, SIDIS provides access to Transverse Momentum Dependent distributions (TMDs), revealing the confined motion of quarks and gluons.

1.3.4 Gluon Saturation and Color Glass Condensate (CGC)

At very high energies (low Bjorken-x), the density of gluons is expected to saturate, forming a novel state of matter known as the Color Glass Condensate (CGC) [18], as depicted in Figure 1.8.

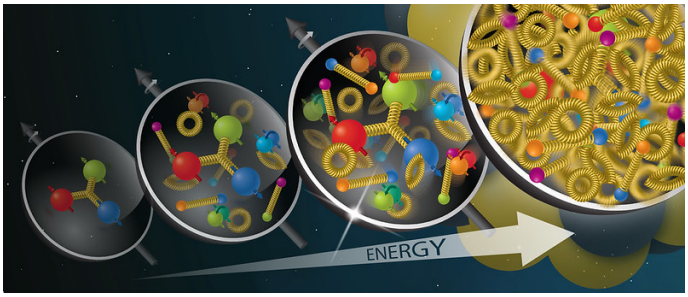

Figure 1.8: Conceptual illustration of the transition from a dilute parton gas at high x to a dense state of saturated gluons, the Color Glass Condensate (CGC), at small x. [1]

- **Process:** Electron-nucleus collisions ($e + A$, e.g., using Au) enhance the gluon density by a factor of $A^{1/3}$, making saturation effects visible at EIC energies.
- **Experimental Approach:**
  - **Di-hadron correlations:** In standard scattering, two hadrons are produced back-to-back. In the CGC state, multiple scatterings with the dense gluon field suppress this angular correlation (disappearance of the back-to-back peak).
  - **Diffractive scattering:** The measurement of coherent diffractive events, where the nucleus remains intact, probes the "black disk" limit of strong interactions.

1.4 The ePIC Experiment and Detector Requirements

To realize these diverse experimental measurements, the ePIC experiment is being developed as the project's primary detector system. The ePIC detector is a general-purpose spectrometer designed to accommodate the wide range of EIC physics processes (Figure 1.9). The current status of the ePIC collaboration and detector integration was extensively discussed at the collaboration meeting in January 2026 [3].

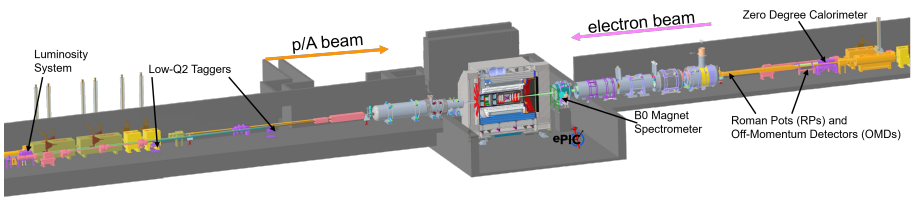

Figure 1.9: Cutaway view of the ePIC detector, showing the various sub-detector systems including tracking, particle identification, and calorimetry, arranged around the interaction point. [3]

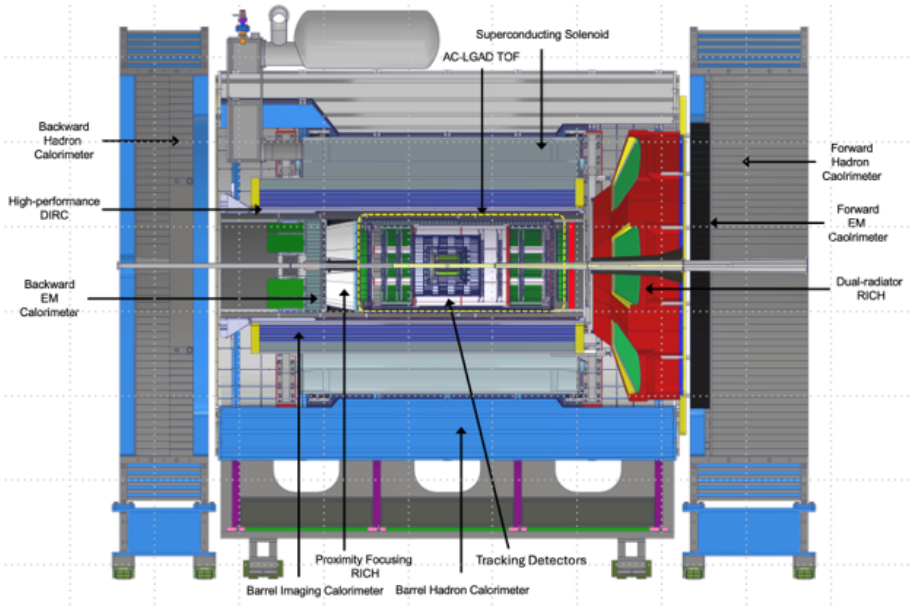

Figure 1.10: Schematic layout of the ePIC detector, highlighting key subsystems such as the tracking detectors, particle identification systems (RICH, DIRC, TOF), and calorimeters, optimized for EIC physics measurements. [2]

The physics goals impose stringent requirements on the detector system, as highlighted in the recent project detector report [2]:

1. **Hermeticity:** To reconstruct the event kinematics (Q^2, x) accurately, the detector must cover a wide acceptance.
2. **Far-Forward Detection:** Detecting recoil protons from DVCS requires dedicated detectors integrated into the beamline.
3. **Particle Identification (PID):** Separating pions, kaons, and protons is mandatory for flavor tagging in SIDIS over a wide momentum range.

1.5 Barrel Time-of-Flight (BTOF) Detector

Within the ePIC detector system, the Barrel Time-of-Flight (BTOF) detector plays a pivotal role in particle identification (PID) in the central region. The BTOF is located between the central tracking system and the electromagnetic calorimeter at a radius of approximately 0.64 m from the beam line. It spans a length of ~ 2.8 m and covers the pseudorapidity range of $-1.33 < \eta < 1.74$ [12]. The total surface area of the detector is approximately $12\,\mathrm{m}^2$, comprising about 2.4 million readout channels.

The primary physics goal of the BTOF is to identify charged hadrons in the low-to-intermediate momentum region, which is critical for measuring decay products

from Heavy Flavor hadrons. Simulation studies based on a total timing resolution of $\sim$ 35–45 ps indicate that the BTOF can achieve a 3σ separation for π/K up to 1.26 GeV/c and for K/p up to 2.09 GeV/c. This capability complements the High-Performance DIRC (hpDIRC), which covers the higher momentum range, ensuring continuous PID coverage across the central barrel.

Meeting these simultaneous requirements presents a significant technological challenge. To achieve the necessary performance, the AC-coupled Low Gain Avalanche Detector (AC-LGAD) has been selected as the baseline technology. The sensor design for the BTOF features strips with dimensions of $0.5 \times 10\,\text{mm}^2$ arranged with a 0.5 mm pitch on a 50 μm thick active volume. This technology offers several key advantages:

- **Precision Timing:** It satisfies the system timing requirement (typically $\sigma_{\text{tot}} \approx 35$ ps) necessary for the momentum limits mentioned above.
- **100% Fill Factor:** Unlike conventional DC-LGADs, which require inter-pad dead zones to prevent breakdown, AC-LGADs utilize a continuous gain layer and AC-coupled readout electrodes, enabling uniform detection efficiency across the sensor surface.
- **Spatial Resolution:** The sensor provides a spatial resolution of $\mathcal{O}(10)$ μm through charge sharing between electrodes. This fine spatial resolution assists the tracking system and helps minimize the material budget by reducing the need for additional tracking layers.

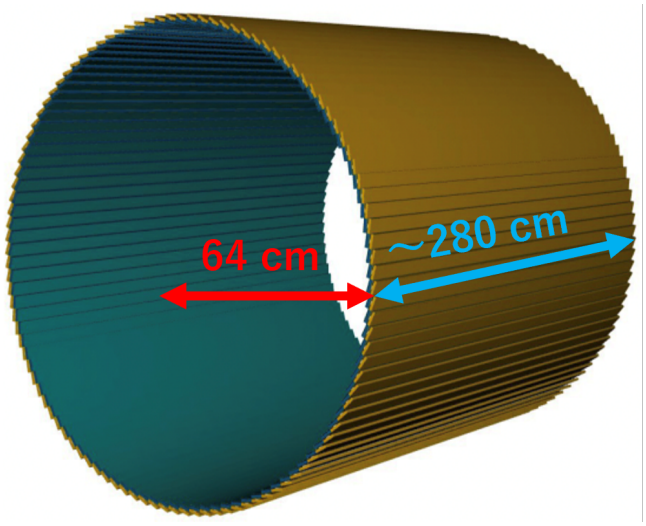

Figure 1.11: Schematic view of the AC-LGAD based TOF system in ePIC. The Barrel TOF (BTOF) is located at $R \approx 0.64$ m, covering $-1.33 < \eta < 1.74$. The system relies on strip-type AC-LGAD sensors to provide both timing and spatial information [4].

1.6 Thesis Objective

As AC-LGAD is a nascent technology, its performance verification and system integration are active areas of research. The primary objective of this thesis is to establish a comprehensive performance evaluation system for AC-LGAD sensors at Hiroshima University and to characterize the sensor properties relevant to the EIC-BTOF requirements.

In this study, I construct an experimental setup utilizing a ^{90}Sr beta source and a high-bandwidth readout system. I focus on:

1. Investigating the temperature dependence of the leakage current and breakdown voltage.
2. Optimizing the bias voltage and signal-to-noise ratio (SNR).
3. Evaluating the charge sharing characteristics essential for position reconstruction.
4. Demonstrating the timing resolution performance required for the BTOF.

This work contributes to the fundamental understanding of AC-LGADs and serves as a step towards the construction of the ePIC BTOF detector.

Chapter 2

Physics and Detector Technology

This chapter provides the theoretical background necessary to understand the operation of the AC-LGAD. We begin with the fundamental interaction of charged particles with matter, focusing on the energy loss mechanisms. Subsequently, we describe the operating principles of standard silicon detectors and the gain mechanism in Low Gain Avalanche Detector (LGAD). Finally, we detail the structure and signal generation mechanism of the AC-LGAD, highlighting its advantages for high-precision 4D tracking required for the EIC experiment.

2.1 Interaction of Particles with Matter

When a charged particle traverses a semiconductor material like silicon, it loses energy primarily through inelastic collisions with atomic electrons, leading to ionization and excitation.

2.1.1 Energy Loss Mechanism

The mean energy loss per unit path length, $-\langle dE/dx \rangle$, is described by the Bethe-Bloch formula:

$$-\left\langle \frac{dE}{dx} \right\rangle = Kz^2 \frac{Z}{A} \frac{1}{\beta^2} \left[\frac{1}{2} \ln \frac{2m_e c^2 \beta^2 \gamma^2 T_{\max}}{I^2} - \beta^2 - \frac{\delta(\beta\gamma)}{2} \right] \tag{2.1}$$

where K is a constant, z is the charge of the incident particle, Z and A are the atomic number and atomic mass of the absorber, β and γ are relativistic kinematic variables, I is the mean excitation energy, and $T_{\max}$ is the maximum kinetic energy transfer in a single collision [19].

In thin silicon sensors (typically tens to hundreds of μm), the energy loss distribution does not follow a Gaussian but is better described by a Landau distribution due to the rare but large energy transfers (delta rays) [5].

2.1.2 Signal Generation in Silicon

In silicon, the average energy required to create an electron-hole pair is approximately 3.6 eV. For a Minimum Ionizing Particle (MIP), the most probable energy loss in 300 μm thick silicon generates about 24,000 electron-hole pairs. These charge carriers drift under an applied electric field, inducing a current on the readout electrodes.

2.2 Standard Silicon Detectors and LGAD

2.2.1 Standard Silicon Detectors (PIN Diodes)

Standard silicon detectors typically utilize a PIN diode structure (p-n junction with an intrinsic region).

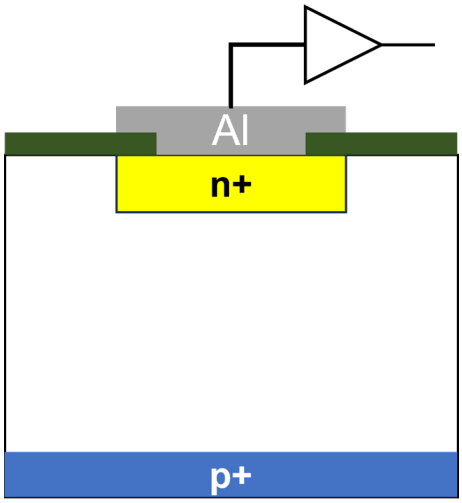

Figure 2.1: Basic structure of a silicon pad detector (PIN diode) where the ionization signal is collected by the electrodes.

When a reverse bias voltage V_{bias} is applied, the depletion region width W expands. For an abrupt junction, W is given by:

$$W \approx \sqrt{\frac{2\epsilon_{Si} V_{\text{bias}}}{q N_{\text{eff}}}} \tag{2.2}$$

where ϵ_{Si} is the permittivity of silicon, q is the elementary charge, and N_{eff} is the effective doping concentration of the bulk [20]. The detector capacitance C_{det}, which dominates the series noise, is inversely proportional to the depletion width ($C_{\text{det}} \propto 1/W$). Thus, full depletion is desirable to minimize noise.

The signal current $i(t)$ induced by the drifting carriers is described by the Shockley-Ramo theorem [21, 22]:

$$i(t) = q\vec{v}(t) \cdot \vec{E}_w(\vec{r}(t)) \tag{2.3}$$

where $\vec{v}(t)$ is the instantaneous velocity of the charge carrier and $\vec{E}_w$ is the weighting field determined by the electrode geometry. While PIN diodes offer excellent spatial resolution, they lack an internal gain mechanism, limiting the time resolution to $\mathcal{O}(100)$ ps due to the low Signal-to-Noise (S/N) ratio and jitter.

2.2.2 Low Gain Avalanche Detector (LGAD)

To improve time resolution, Low Gain Avalanche Detector (LGAD) incorporates an internal gain mechanism [23]. An additional p-type doping layer (Gain Layer) is inserted just below the n-type cathode.

Gain Mechanism

When a high reverse bias voltage is applied, the electric field in the gain layer becomes high enough ($E > 3 \times 10^5$ V/cm) to trigger impact ionization. Electrons drifting from the bulk into this high-field region gain sufficient kinetic energy to knock out secondary electrons, creating an avalanche effect. The multiplication factor (Gain, G) is determined by the ionization coefficient α, which depends exponentially on the electric field:

$$G = \exp\left(\int_0^d \alpha(E(x))dx\right) \tag{2.4}$$

where d is the thickness of the gain layer.

Temperature Dependence

The ionization coefficient α is strongly dependent on temperature. As the temperature increases, phonon scattering becomes more frequent, reducing the mean free path of the carriers. Consequently, carriers require a higher electric field to reach the ionization threshold energy [24]. This implies that for a fixed bias voltage, the gain decreases as temperature rises. Therefore, precise temperature control is essential for the stable operation of LGADs in experimental environments.

Typical LGAD achieves a gain of 10–50, significantly improving the S/N ratio and reducing timing jitter ($\sigma_j \propto N/(dV/dt)$), enabling time resolutions of $\mathcal{O}(30)$ ps.

2.2.3 Limitations of DC-LGAD

In conventional LGAD (DC-LGAD), readout pixels must be physically separated by structures such as Junction Termination Extensions (JTE) to prevent breakdown. These inter-pixel regions act as "dead zones" where no amplification occurs (Figure 2.2). As the pixel pitch decreases, the fill factor (detection efficiency) drops significantly. This trade-off makes it difficult to achieve both high spatial resolution and high detection efficiency simultaneously with DC-LGAD.

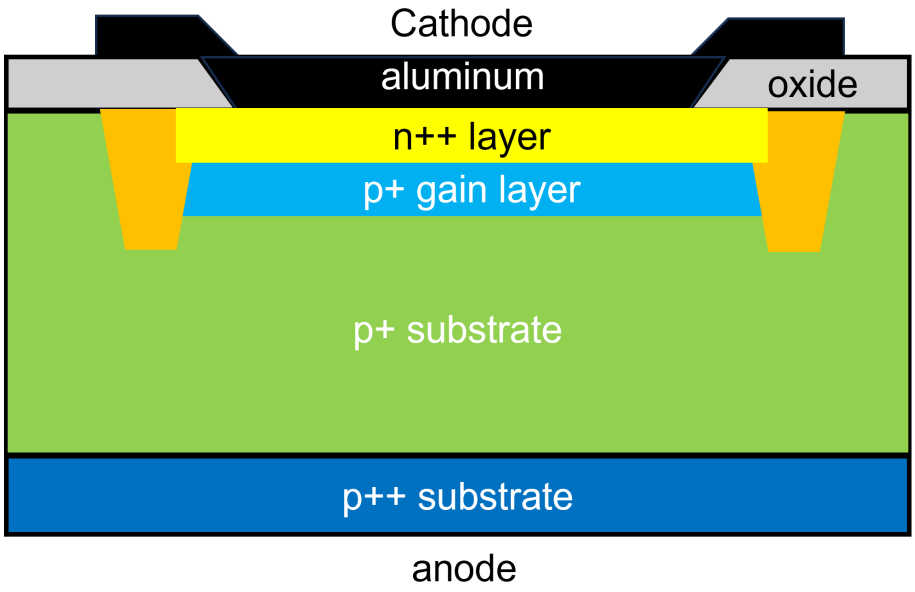

Figure 2.2: Cross-sectional schematic of a standard DC-LGAD. The Junction Termination Extension (JTE) and p-stop structures between pixels create dead zones where charge multiplication does not occur, reducing the fill factor.

2.3 Principle of AC-LGAD

2.3.1 Structure and AC-Coupling

The AC-coupled LGAD (AC-LGAD), also known as the Resistive Silicon Detector (RSD), is designed to overcome the fill factor limitation of DC-LGAD while maintaining excellent timing performance. Recent developments and reviews highlight its capability to achieve both high spatial and time resolutions, making it a prime candidate for next-generation 4D tracking [25, 26].

Its key structural features are shown in Figure 2.3:

1. **Continuous Gain Layer:** The gain layer and the n^+ resistive layer are continuous across the entire sensor active area. This continuous structure

eliminates the inter-pixel dead zones found in DC-LGAD, ensuring a 100% fill factor [26].

2. **Dielectric Layer:** A thin insulating oxide layer acts as a coupling capacitor (C_{coupling}).

3. **AC-Coupled Electrodes:** Metal readout pads (or strips) are patterned on top of the oxide layer.

Signals generated by the avalanche process in the bulk are capacitively coupled (AC-coupled) from the continuous resistive layer to the metal readout pads.

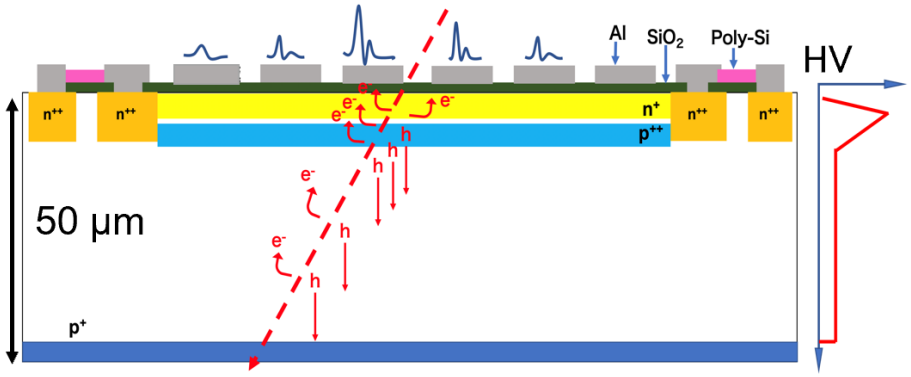

Figure 2.3: Cross-sectional schematic of an AC-LGAD. The continuous gain and resistive layers provide a 100% fill factor. Signals are capacitively coupled to the metal electrodes through the oxide layer.

2.3.2 Charge Sharing Mechanism

Unlike DC-LGADs, the signal in AC-LGADs is not collected directly but is induced capacitively through the oxide layer. A unique feature is the "charge sharing" phenomenon governed by the resistive n^+ layer [27].

The electrons from the avalanche collect at the resistive n^+ layer and spread laterally. The signal induced on a specific pad depends on the impedance path—determined by the sheet resistance (R_{sheet}) and the distance from the hit position to the pad. This allows the signal to be shared among multiple adjacent electrodes. By analyzing the ratio of signal amplitudes on neighboring pads (e.g., using the center of gravity method), precise position reconstruction is possible.

Even with a large electrode pitch (e.g., 500 μm), a spatial resolution of $\mathcal{O}(10)$ μm can be achieved [27]. Thus, AC-LGADs successfully combine the high time resolution of LGADs with the high spatial resolution required for 4D tracking.

2.4 AC-LGAD Sensors for EIC

In the ePIC detector at the Electron-Ion Collider (EIC), AC-LGAD technology is adopted for the Time-of-Flight (TOF) systems to provide charged particle identification (PID) and timestamping. Two different electrode geometries are employed depending on the detector region:

- **Forward TOF (FTOF):** Located in the forward endcap region, the FTOF utilizes **pixel-type AC-LGADs** (Figure 2.4) to handle high particle occupancy and provide precise tracking in a high-rate environment.
- **Barrel TOF (BTOF):** Located in the central barrel region, the BTOF utilizes **strip-type AC-LGADs** (Figure 2.5). The strip geometry allows for covering a large area cost-effectively while maintaining sufficient spatial resolution through charge sharing.

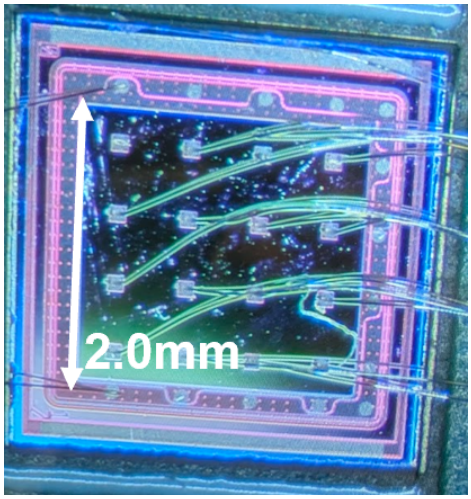

Figure 2.4: Photograph of a pixel-type AC-LGAD prototype designed for the FTOF region.

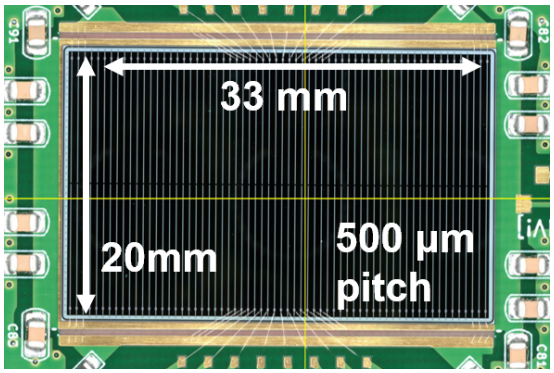

Figure 2.5: Photograph of the HPK strip-type AC-LGAD used in this study, designed for the BTOF region.

2.4.1 Sensor Specification for This Study

For the evaluation presented in this thesis, we utilized a **strip-type AC-LGAD** manufactured by **Hamamatsu Photonics K.K. (HPK)**. This sensor is designed with the same specifications as the production model planned for the BTOF.

The key parameters of the sensor are summarized in Table 2.1.

Figure 2.5 shows the layout and a photograph of the strip AC-LGAD used in this study. The evaluation of this specific sensor is crucial for verifying the performance of the BTOF system in the EIC.

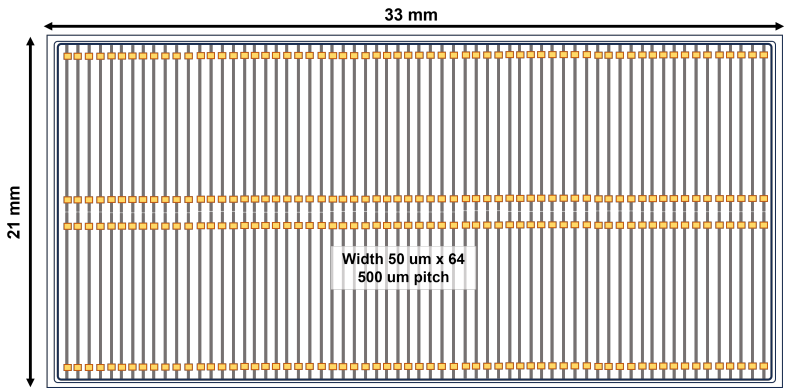

Figure 2.6: Detailed layout of the strip-type AC-LGAD sensor showing a 500μm pitch and 20×33 mm active area.

Table 2.1: Key parameters of the AC-LGAD sensor utilized in this study.

Parameter	**Specification**
Type	AC-coupled Strip LGAD
Substrate Thickness	50 μm (active thickness)
Strip Pitch	500 μm
Strip Length	≈ 20 mm (Dimensions: 20×33 mm)

Chapter 3

Experimental Setup

This chapter details the construction of the comprehensive performance evaluation system established at Hiroshima University. To precisely characterize the AC-LGAD sensors, the system was designed with three key requirements: a high-precision timing reference, rigorous environmental control to stabilize the avalanche gain, and a wide-bandwidth readout system. The setup is versatile and capable of evaluating various sensor prototypes for the EIC-ePIC experiment.

3.1 Overview of the Evaluation System

The primary objective of this experimental setup is to establish a high-fidelity measurement environment capable of extracting the intrinsic performance of the AC-LGAD sensor. To achieve this, a comprehensive system was designed not only to record signals but also to strictly control environmental variables and ensure signal integrity. Figure 3.1 illustrates the schematic view of the experimental layout.

The measurement system is designed to acquire raw analog waveforms from both the AC-LGAD (Device Under Test) and the reference PMT. This full-waveform readout is essential for the detailed offline analysis required to understand the complex signal characteristics of the sensor. Furthermore, to investigate the temperature dependence of the sensor's behavior, the DUT and the reference detector are housed within a **constant-temperature bath**. This allows for data acquisition across a strictly controlled temperature range, which is crucial for characterizing the device's stability and gain variations.

Operational efficiency and reproducibility were also prioritized. The High Voltage (HV) bias applied to the AC-LGAD is controlled via an online remote system. This implementation simplifies the voltage configuration process and ensures precise logging of the bias conditions for every dataset. Finally, special attention was paid to the signal transmission lines to minimize experimental artifacts. High-quality cables

were selected to ensure low latency and negligible signal degradation, preserving the integrity of the fast transient signals output by the AC-LGAD.

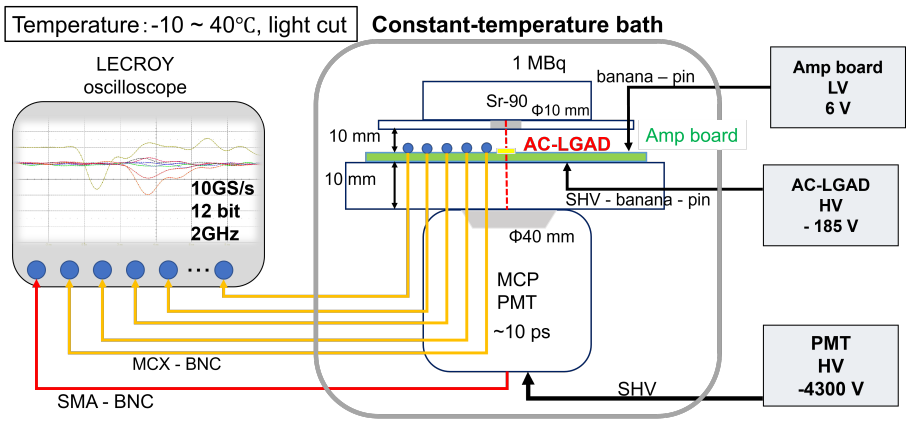

Figure 3.1: Schematic diagram of the AC-LGAD performance evaluation system. The setup includes a ^{90}Sr beta source, a constant-temperature bath for temperature control, an AC-LGAD sensor as the Device Under Test (DUT), a reference MCP-PMT for timing, and a high-bandwidth oscilloscope for waveform acquisition.

3.2 Beta Source and Trigger System

To simulate minimum ionizing particles (MIPs) expected in the actual experiment, we utilized a Strontium-90 (^{90}Sr) beta source with an activity of 1 MBq [28]. The electrons emitted from the source pass through the AC-LGAD (DUT) and impinge on the trigger detector placed downstream.

Figure 3.2: Photograph of the ^{90}Sr beta source used in the experiment. The source emits high-energy electrons that mimic MIP-like events for sensor characterization.

3.2.1 Reference Timing Detector

To evaluate the timing performance of the AC-LGAD, a Multi-Anode Micro-Channel Plate Photomultiplier Tube (MCP-PMT) manufactured by Photek was selected as the reference timing detector.

MCP-PMTs are distinguished by their use of a micro-channel plate for electron multiplication, which enables significantly faster response times compared to conventional photomultiplier tubes. According to the manufacturer's specifications, these devices are characterized by an ultra-fast rise time and an exceptionally low Transit Time Spread (TTS), typically in the range of tens of picoseconds [29]. The multi-anode architecture allows for spatial resolution, but in this experimental setup, the device is primarily utilized for its superior timing properties to provide a precise "start" timestamp for the incident particles.

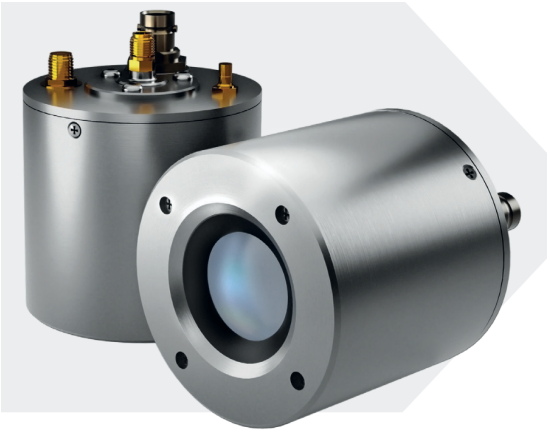

(a) Image of the MCP-PMT used as the reference detector.

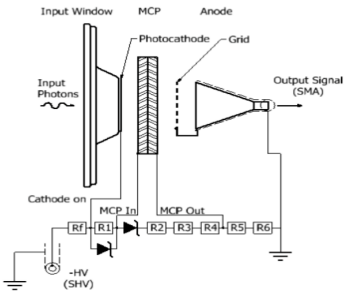

(b) Schematic layout of the MCP-PMT internal structure.

Figure 3.3: (a) Photograph of the MCP-PMT reference detector. (b) Schematic diagram illustrating the internal structure of the MCP-PMT, highlighting the micro-channel plates responsible for electron multiplication.

The importance of the reference detector's time resolution cannot be overstated in this analysis. The total measured time resolution of the system, σ_{total}, is the quadratic sum of the intrinsic resolution of the Device Under Test (DUT), σ_{DUT}, and the reference detector, σ_{Ref}:

$$\sigma_{\text{total}} = \sqrt{\sigma_{\text{DUT}}^2 + \sigma_{\text{Ref}}^2} \tag{3.1}$$

Since the AC-LGAD is expected to have a high time resolution of approximately 30–40 ps, using a reference detector with comparable or inferior resolution would dominate the measurement error, making it impossible to extract the true performance of the DUT. The Photek MCP-PMT used in this system provides an intrinsic time resolution of approximately 10 ps. This minimal contribution ($\sigma_{\text{Ref}} \ll \sigma_{\text{DUT}}$) ensures that the measured timing distribution is dominated by the AC-LGAD's characteristics, thereby allowing for an accurate and reliable evaluation of the sensor's intrinsic timing capabilities.

3.3 Environmental Control

The gain of an LGAD is highly sensitive to temperature because the impact ionization coefficients of electrons and holes depend on the lattice temperature. Precise temperature control is therefore mandatory for stable operation and reliable characterization.

I installed the setup inside a light-tight constant-temperature bath capable of regulating the temperature from $-10°C$ to $+40°C$. This capability allows us to:

1. Evaluate the temperature dependence of the leakage current and breakdown voltage.
2. Study the variation of signal gain as a function of temperature.
3. Simulate the expected operating temperature at the EIC (typically around $20°C$ to $30°C$).

Regarding temperature monitoring, although the readout board for the DUT is equipped with an onboard temperature sensor, it was not utilized in this experiment due to limitations in the data acquisition interface. Instead, the internal temperature of the constant-temperature bath was treated as the sensor temperature, ensuring that sufficient waiting time was provided for the system to reach thermal equilibrium before each measurement.

(a) Outside view of the constant-temperature bath housing the AC-LGAD and reference detector.

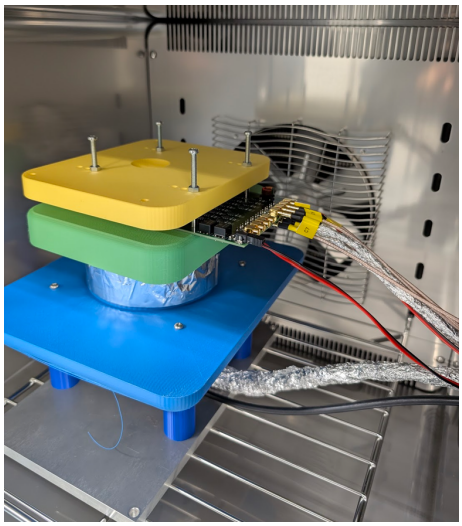

(b) Inside view of the constant-temperature bath showing the AC-LGAD and MCP-PMT mounted on the test bench.

Figure 3.4: (a) Photograph of the constant-temperature bath used for environmental control. (b) Interior view of the chamber with the AC-LGAD sensor and MCP-PMT reference detector mounted on the test bench.

3.4 Readout Electronics and Data Acquisition

3.4.1 Front-end Electronics

The AC-LGAD sensor is mounted on a custom-designed 16-channel readout board developed at Fermi National Accelerator Laboratory (FNAL), as shown in Figure 3.5. This board is specifically engineered to handle the fast transient signals characteristic of LGADs.

Key features of the readout board include:

- **Sensor Mounting:** The AC-LGAD is placed in the center of the PCB, with its electrodes wire-bonded directly to the amplifier inputs to minimize parasitic inductance.
- **Signal Readout:** The board provides 16 independent analog output channels. The signals are read out through MCX connectors located on the right edge of the board, divided into two groups: 8 channels for the top row and 8 channels for the bottom row.
- **Power Supply:** Two distinct power inputs are required. A High Voltage (HV) bias is applied to the sensor to generate the internal gain, while a Low Voltage (LV) of 6 V is supplied to power the on-board transimpedance amplifiers.

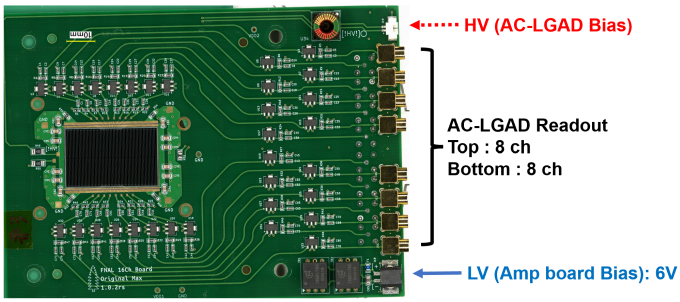

Figure 3.5: Photograph of the 16-channel readout board designed at Fermilab (FNAL).

3.4.2 Data Acquisition (DAQ) System

The amplified signals from the AC-LGAD and the reference signal from the MCP-PMT were fed into a high-performance oscilloscope (LeCroy). The key specifications of the digitizer are:

- **Bandwidth:** 2 GHz (sufficient to capture the fast rise time of LGAD signals).

- **Sampling Rate:** 10 GS/s (providing a data point every 100 ps, enabling precise waveform fitting).
- **Vertical Resolution:** 12-bit (essential for high dynamic range and accurate amplitude measurement).

The oscilloscope was controlled via a PC, and the waveforms were stored for offline analysis. The high voltage units for both the AC-LGAD and the MCP-PMT were also remotely monitored to ensure stability during long-term measurements.

Figure 3.6: Screenshot of the online monitoring interface for the high voltage supply system. This interface allows for remote control and real-time monitoring of the bias voltages applied to both the AC-LGAD sensor and the MCP-PMT reference detector.

Chapter 4

Analysis Method

This chapter describes the data processing and analysis methods used to evaluate the AC-LGAD performance. We first define the signal parameters extracted from the raw waveforms. Then, we outline the strategic workflow adopted in this thesis to determine the optimal operating conditions, including the verification of temperature stability. Finally, we detail the mathematical formulation used to calculate the time resolution, providing a breakdown of its internal components.

4.1 Waveform Processing and Signal Definition

The raw waveform data acquired by the oscilloscope were processed offline. For each event, the following procedures were applied to extract signal characteristics.

4.1.1 Pedestal Subtraction and Noise Evaluation

The baseline level (pedestal) was calculated event-by-event by averaging the voltage samples in a pre-trigger window (typically the first 10 ns of the recorded window). This value was subtracted from the entire waveform to correct for any DC offset. The noise level (σ_{noise}) was defined as the standard deviation (RMS) of the baseline fluctuations in the same pre-trigger window.

4.1.2 Signal Amplitude

The signal amplitude (V_{peak}) is defined as the maximum voltage value of the pulse after pedestal subtraction. Events with amplitudes lower than a specific threshold (typically $5\sigma_{\text{noise}}$) were rejected as noise to ensure data quality.

4.1.3 Timing Extraction (CFD Method)

In timing measurements, the achievable time resolution is fundamentally limited by "time jitter" caused by electronic noise and "time walk" caused by signal amplitude variations. To minimize the contribution of time walk and determine the signal arrival time with high precision, the Constant Fraction Discriminator (CFD) method was employed in this analysis.

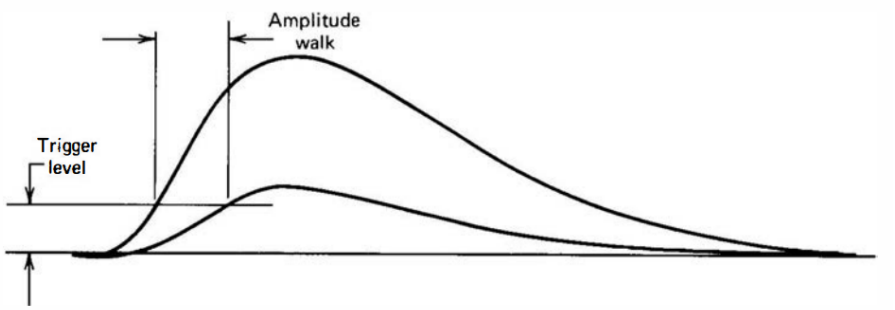

Figure 4.1: Illustration of time walk in a fixed threshold discriminator. Signals with different amplitudes cross the threshold at different times, causing a timing error. (Reprinted from Knoll [5, p.682])

In a conventional fixed-threshold method, signals with different amplitudes cross the threshold at different times, resulting in significant time walk. This effect is particularly detrimental for LGAD sensors, where the signal amplitude varies event-by-event due to the Landau distribution of energy deposition. In contrast, the CFD method defines the trigger point at a constant fraction f of the peak amplitude, making the derived timing ideally independent of the pulse height. The arrival time t_{CFD} is determined as:

$$V(t_{\mathrm{CFD}}) = f \times V_{\mathrm{peak}} \tag{4.1}$$

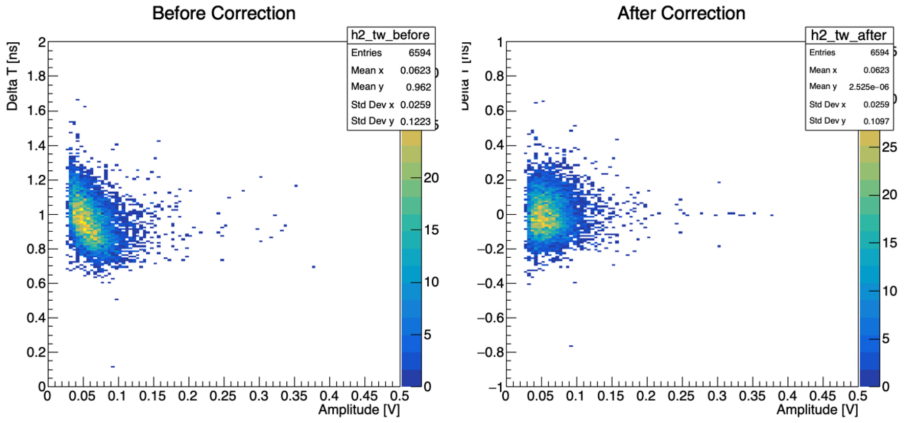

Figure 4.2: Effect of time-walk correction using the CFD method. The left panel shows the correlation between signal amplitude and timing difference (ΔT) before correction (using a fixed threshold), where a clear time-walk effect is visible. The right panel shows the distribution after applying the CFD method. The amplitude dependence is significantly suppressed, and the timing resolution is improved.

In this analysis, a fraction of 50% ($f = 0.5$) was primarily selected to maximize the slew rate at the trigger point, thereby minimizing the jitter contribution. Since the sampling interval of the digitizer is 100 ps, linear interpolation was performed between the two sampling points surrounding the threshold to achieve sub-sample timing precision.

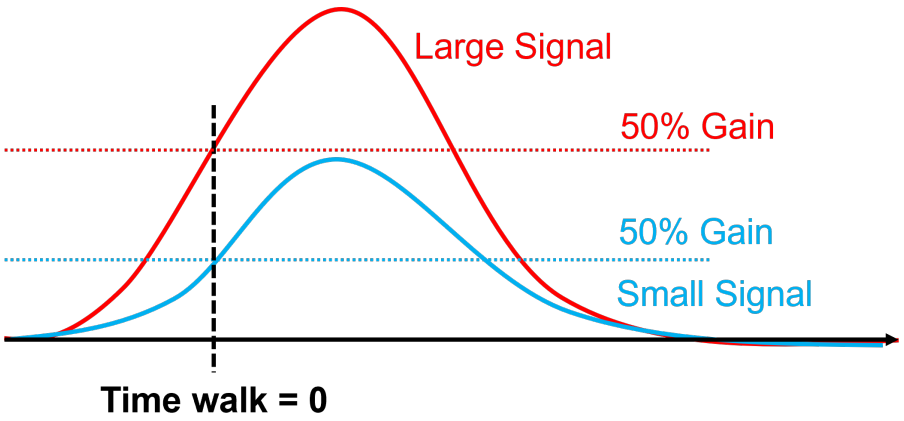

Figure 4.3: Example of timing extraction using the CFD method. The trigger point is determined at 50% of the peak amplitude, and linear interpolation is used to achieve sub-sample timing resolution.

4.2 Strategy for Performance Evaluation

A systematic approach was adopted to evaluate the sensor performance and demonstrate the validity of the evaluation system. The analysis follows the logical flow

described below.

4.2.1 Verification of Temperature Stability

Precise temperature control is essential for LGAD characterization because the avalanche gain is highly temperature-dependent. Although a direct temperature probe was not attached to the sensor surface during the beam/source tests, the sensor temperature was monitored indirectly via the leakage current (I_{leak}), which exhibits a known exponential dependence on temperature.

To validate the stability of the environmental control, a control experiment was conducted comparing the leakage current behavior in an uncontrolled environment versus inside the climate chamber (thermostat).

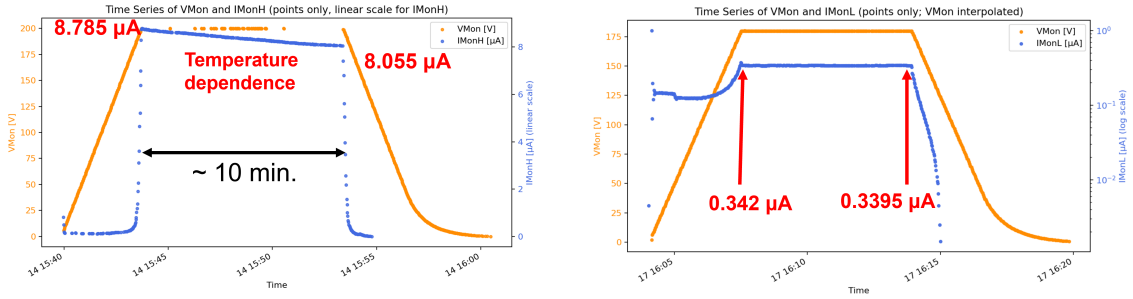

(a) Uncontrolled environment **(b)** Controlled environment (Thermostat)

Figure 4.4: Time series monitoring of leakage current (I_{leak}) and bias voltage (V_{bias}). (a) In an uncontrolled environment, I_{leak} drifted from 8.79 μA to 8.06 μA over 10 minutes due to ambient temperature changes. (b) In the climate chamber used for this study, I_{leak} remained stable (variation $< 1\%$) over the same duration, confirming that the sensor temperature was kept constant.

As shown in Figure 4.4(a), measurement in an open environment resulted in a significant drift in leakage current ($\sim 8\%$ change) over 10 minutes, indicating a fluctuation in sensor temperature. In contrast, Figure 4.4(b) demonstrates that inside the climate chamber, the leakage current remained extremely stable ($0.342\mu\text{A} \rightarrow 0.3395\mu\text{A}$) under constant voltage. This result confirms that controlling the atmospheric temperature in the chamber effectively stabilizes the sensor temperature, ensuring reliable gain characterization.

4.2.2 Determination of Operational Parameters

1. **Basic Characterization (I-V and Noise):**
   First, the leakage current was measured as a function of bias voltage (I-V curve) at various temperatures using a CAEN high-voltage power supply controlled by the "CAENGECO2020" software (1 Hz logging rate).

To validate this monitoring method, the obtained I-V characteristics were compared with reference measurements provided by the manufacturer (HPK) and probe station data (Figure 4.5). Although the monitoring system tends to output higher current values in the low-voltage region due to transient effects (Fig. 4.5(d)), the behavior near the breakdown voltage is consistent with the reference data (Fig. 4.5(a) and (b)). This confirms that the system accurately captures the steady-state behavior necessary for determining the operational bias voltage.

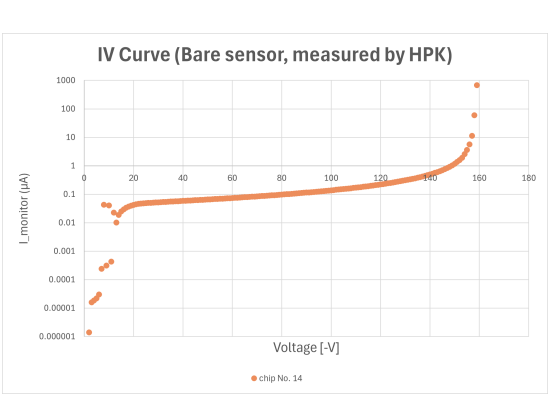

(a) HPK data sheet (bare sensor)

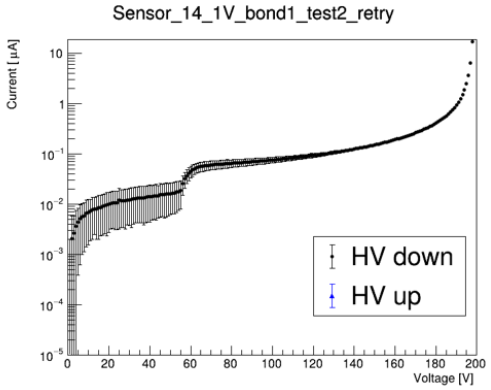

(b) Probe station measurement (wire-bonded)

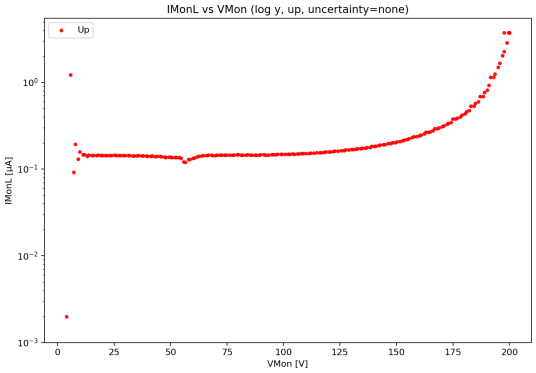

(c) Log file output at 20°C

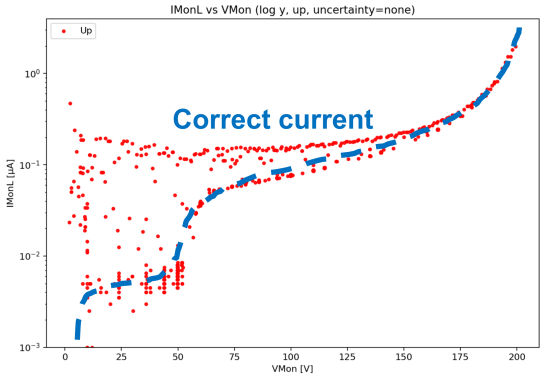

(d) Raw monitoring data including transient currents

Figure 4.5: Comparison of I-V characteristics of the AC-LGAD sensor. (a) Measurement result provided by HPK. (b) Measurement at a probe station after wire-bonding. (c) Steady-state I-V curve extracted from the log file at 20°C. (d) Raw monitoring data. The scatter reflects transient currents recorded due to the sampling interval during voltage steps.

Measurements were subsequently conducted across multiple temperature points to characterize the temperature dependence. The breakdown voltage at room temperature (20°C) serves as a baseline to determine the operational range and to quantify the shift in gain characteristics.

2. **Signal-to-Noise Ratio (SNR) Analysis:**
   To identify the voltage region where the signal is sufficiently distinguishable

from the background noise, the Signal-to-Noise Ratio (SNR) is analyzed as a function of bias voltage for each temperature. The SNR is calculated using the following equation:

$$\mathrm{SNR} = \frac{V_{\mathrm{peak}}}{\sigma_{\mathrm{noise}}} \tag{4.2}$$

where V_{peak} is the mean signal amplitude (MPV or Gaussian mean) and σ_{noise} is the RMS noise level. This step is crucial because the time resolution is theoretically proportional to the inverse of the SNR ($\sigma_t \propto 1/\mathrm{SNR}$).

3. **Determination of Optimal Bias Voltage ($V_{\mathbf{opt}}$):**
   The optimal bias voltage is defined to balance high gain (high SNR) with operational stability. In this study, we define the **Breakdown Voltage ($V_{\mathbf{bd}}$)** as the voltage where the leakage current exceeds 1μA:

$$I_{\mathrm{leak}}(V_{\mathrm{bd}}) \equiv 1\mu\mathrm{A} \tag{4.3}$$

   Operating at V_{bd} poses a risk of instability. Therefore, the optimal voltage V_{opt} is set with a safety margin of $5 \sim 10$ V:

$$V_{\mathrm{opt}} = V_{\mathrm{bd}} - (5 \sim 10)\,\mathrm{V} \tag{4.4}$$

   This definition ensures that the sensor operates in a high-gain region while maintaining a safe margin against thermal runaway or breakdown.

4.3 Calculation and Breakdown of Time Resolution

The total time resolution of the system (σ_{total}) is evaluated using the distribution of the time difference (Δt) between the AC-LGAD (DUT) and the reference detector (MCP-PMT):

$$\sigma_{\mathrm{total}} = \sqrt{\sigma_{\mathrm{DUT}}^2 + \sigma_{\mathrm{Ref}}^2 + \sigma_{\mathrm{RO}}^2} \tag{4.5}$$

where σ_{DUT}, σ_{Ref}, and σ_{RO} correspond to the resolutions of the AC-LGAD, the reference detector, and the readout electronics, respectively. Based on the reference detector specifications and calibration, $\sigma_{\mathrm{Ref}} \approx 10$ ps and $\sigma_{\mathrm{RO}} \approx 10$ ps.

4.3.1 Components of AC-LGAD Resolution

The intrinsic time resolution of the AC-LGAD (σ_{DUT}) can be further decomposed into three physical components:

$$\sigma_{\mathrm{DUT}}^2 = \sigma_{\mathrm{intr}}^2 + \sigma_{\mathrm{jitter}}^2 + \sigma_{\mathrm{tw}}^2 \tag{4.6}$$

- **Jitter (σ_{jitter}):** Caused by electronic noise superimposed on the signal. It is defined as $\sigma_{\text{jitter}} = \sigma_{\text{noise}}/(dV/dt) \approx t_{\text{rise}}/\text{SNR}$. In this study, the high SNR allows this term to be suppressed to approximately 10 ps.
- **Time Walk (σ_{tw}):** Caused by amplitude variations. As described in Section 4.1.3, the use of the CFD method renders this component negligible ($\sigma_{\text{tw}} \approx 0$).
- **Intrinsic Resolution (σ_{intr}):** This is the fundamental limit determined by the physics of the sensor, specifically the **Landau fluctuations**. The non-uniform charge deposition along the particle track creates statistical fluctuations in the time it takes for carriers to reach the gain layer and initiate the avalanche.

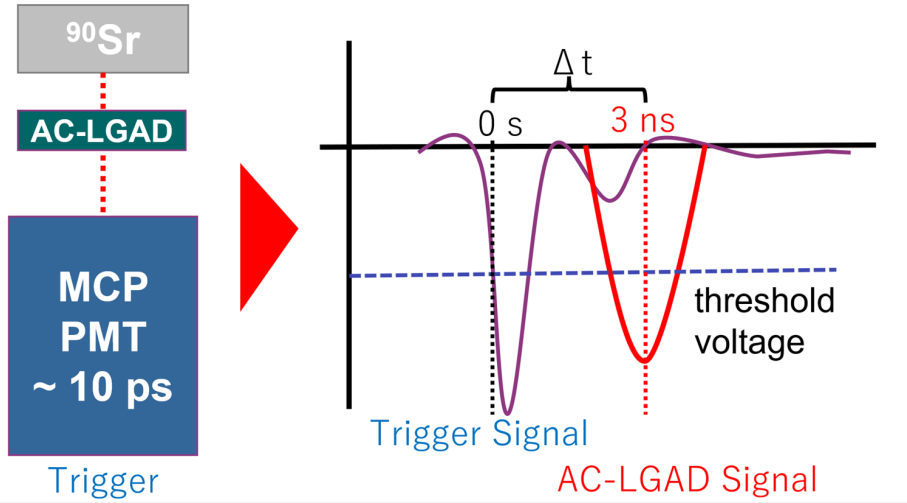

Figure 4.6: Schematic illustration of time resolution calculation using the time difference between the DUT and reference detector.

4.4 Position Estimation via Charge Sharing

To verify the unique signal induction mechanism of the AC-LGAD, the impact position of the incident particle is estimated using the charge sharing characteristics. Unlike standard sensors where the signal is localized to a single electrode, the AC-LGAD induces signals on multiple adjacent strips depending on the hit position.

In this analysis, the approximate hit position x_{hit} is estimated by calculating the weighted centroid of the signal amplitudes across the relevant strips. The position is defined as:

$$x_{\text{hit}} = \frac{\sum_i w_i x_i}{\sum_i w_i} \tag{4.7}$$

where:

- w_i represents the gain (integrated charge or amplitude) of the i-th strip.
- x_i denotes the position of the i-th strip (defined at the center of each strip).

It is important to note that in this experimental setup, the exact true hit position of the incident electrons is not known. Therefore, the precise position resolution cannot be derived from this specific measurement. Instead, this analysis serves to qualitatively verify the charge sharing feature of the AC-LGAD. Specifically, it demonstrates that hit positions can be reconstructed continuously between strips, confirming that the sensor is sensitive to the impact location beyond the granularity of the strip pitch.

Figure 4.7 shows a representative waveform event where signals are induced on multiple strips. As seen in the figure, the signal is shared between adjacent channels, providing the necessary amplitude information (w_i) for the weighted centroid calculation described above.

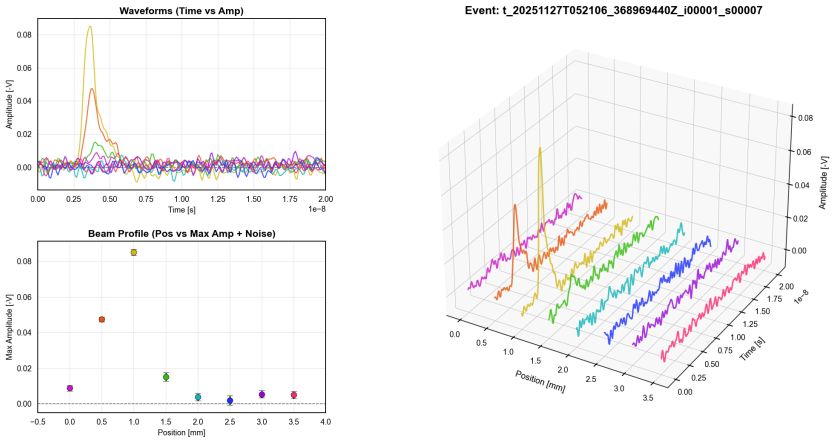

Figure 4.7: A representative event display demonstrating charge sharing. Signals are induced on adjacent strips, and their amplitudes are used as weights (w_i) to estimate the hit position via the centroid method.

Chapter 5

Results

In this chapter, we present the comprehensive performance evaluation of the AC-LGAD prototype, conducted using the newly constructed β-source evaluation system. The primary objective is to validate the precision of the experimental setup while characterizing the fundamental properties of the sensor for the EIC-ePIC BTOF detector. The analysis proceeds in three main steps: first, we assess the basic electrical characteristics, focusing on the temperature dependence of the breakdown voltage. Second, we determine the optimal bias voltage by analyzing the trade-off between Signal-to-Noise Ratio (SNR) and operational stability. Finally, we report the intrinsic time resolution and the position reconstruction performance, including the application of linearity corrections. Detailed physical interpretations of these results are discussed in Chapter 6.

5.1 Basic Characterization

5.1.1 Current-Voltage (I-V) Characteristics

The leakage current is a fundamental parameter indicative of sensor quality and the onset of avalanche multiplication. Figure 5.1 shows the I-V characteristics of the AC-LGAD measured across a temperature range of $-10°$C to $+40°$C, focusing on the behavior near the breakdown region.

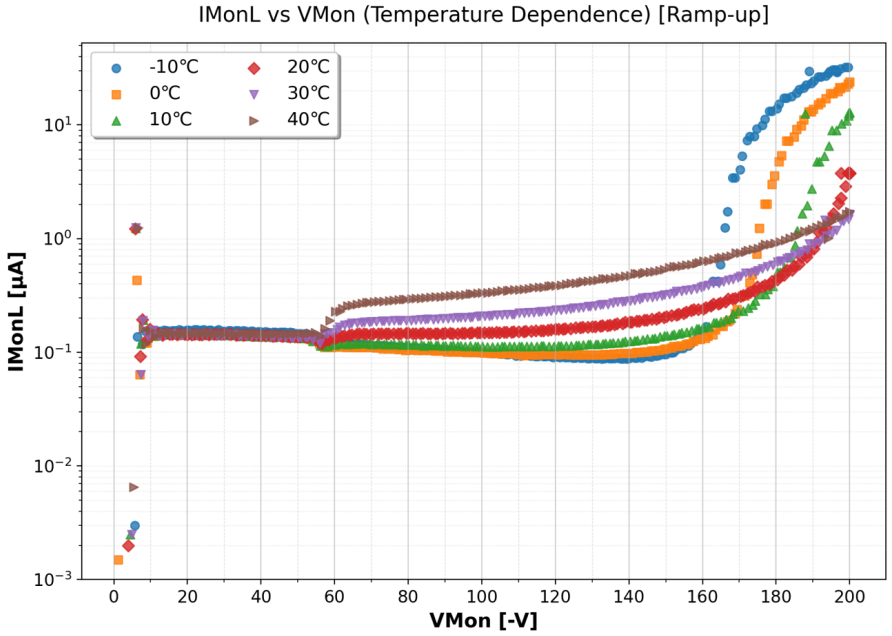

Figure 5.1: Current-Voltage (I-V) characteristics measured at different temperatures. The horizontal dotted line represents the 1 μA threshold used for stability assessment.

General Features of the I-V Curve

The measured I-V curves exhibit several distinct features characteristic of LGADs:

- **Shoulder at ~ -60 V:** A slight increase in current is observed around -60 V. This feature corresponds to the voltage where the gain layer and the bulk are fully depleted. Beyond this point, the current is dominated by bulk generation.
- **Breakdown Voltage Shift:** The voltage at which the current rises sharply (avalanche breakdown) shifts significantly with temperature.
- **Thermal Leakage:** At higher temperatures (e.g., +40°C), a substantial increase in thermal leakage current is observed even at low bias voltages, making the determination of a distinct breakdown point difficult.

Temperature Dependence of Breakdown Voltage

To quantify the temperature dependence, the breakdown voltage (V_{bd}) was defined as the voltage where the leakage current exceeds a threshold of 1 μA ($I_{\text{leak}} > 1$ μA). The measured V_{bd} values are listed in Table 5.1.

The data at +40°C was excluded from this analysis because the thermal leakage current exceeded the threshold before the onset of avalanche breakdown.

Table 5.1: Measured breakdown voltages (V_{bd}) at different temperatures.

Temperature [°C]	Breakdown Voltage (V_{bd}) [V]
−10	−166
0	−175
10	−186
20	−190
30	−194

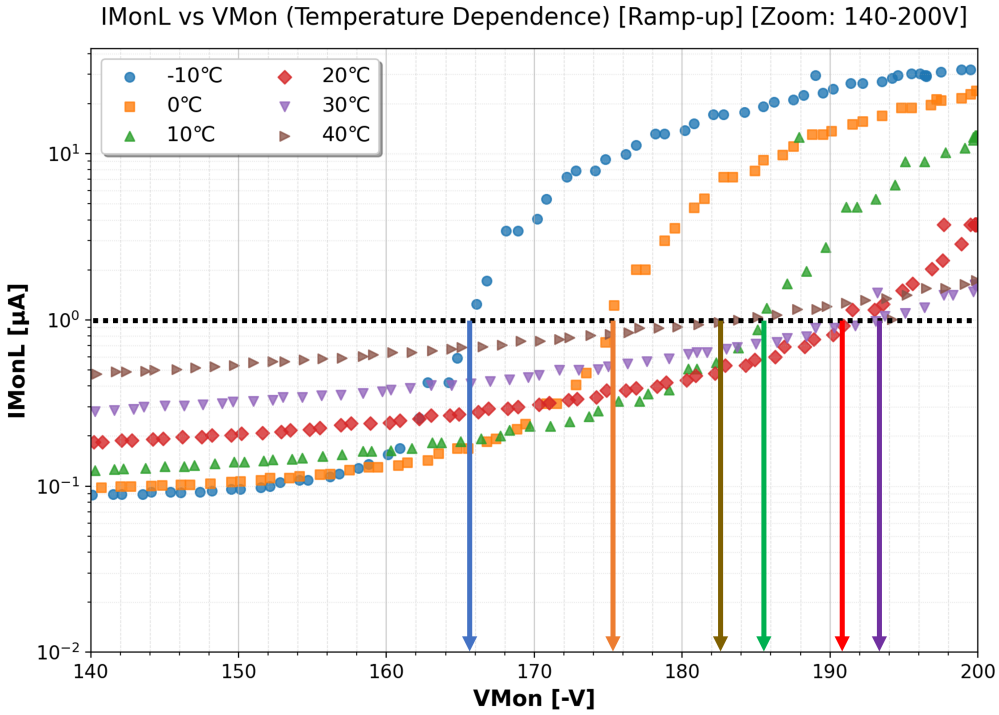

Figure 5.2: Detailed view of I-V characteristics near the breakdown voltage. The breakdown voltage (V_{bd}), defined at 1 μA, shifts towards higher absolute voltages as temperature increases.

Figure 5.2 illustrates the correlation between temperature and breakdown voltage. We applied a linear interpolation using the **Least Squares Method** to the data points from -10°C to 30°C. The relationship is well-described by the linear equation:

$$|V_{bd}(T)| = 0.71T + 175.1 \tag{5.1}$$

where T is the temperature in degrees Celsius. The coefficient of determination was calculated to be $R^2 \approx 0.98$, indicating a strong linear correlation. The physical mechanism behind this positive temperature coefficient and the impact of the "shoulder" feature are discussed in Section 6.1.1.

5.1.2 Noise Level

The noise level is a limiting factor for the timing resolution. The baseline noise (RMS) was evaluated as a function of bias voltage. As shown in the noise analysis (Figure 5.3, right), the noise level generally increases with the bias voltage due to the higher electric field and gain. However, within the stable operation range, the noise level was maintained at a few mV (e.g., $\sim 2.2 - 2.4$ mV at typical operating voltages), confirming the low-noise performance of the readout electronics.

5.2 Signal-to-Noise Ratio and Operating Point Determination

The optimization of the bias voltage is a trade-off between maximizing the signal gain and maintaining detector stability.

5.2.1 Behavior Near Breakdown (0°C Case Study)

To understand the sensor behavior near the breakdown region, we analyzed the signal and noise at 0°C, where the breakdown voltage shifts to a lower value. Figure 5.3 shows the signal amplitude, gain curve, and SNR at 0°C.

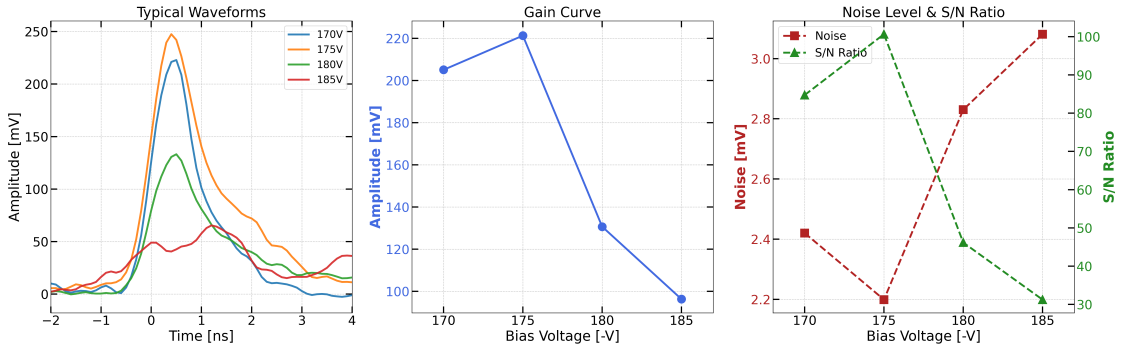

Figure 5.3: Waveform characteristics at 0°C. (Left) Waveform shape, (Center) Signal amplitude vs Bias, (Right) Noise RMS and SNR. Significant variations in SNR are observed due to the proximity to the breakdown voltage.

In the voltage range of −170 V to −185 V at 0°C, the sensor operates close to its breakdown limit. Consequently, slight changes in bias voltage lead to drastic fluctuations in leakage current and noise, causing the SNR to peak and then degrade rapidly. This demonstrates that operating too close to the breakdown voltage introduces instability, where performance becomes overly sensitive to voltage fluctuations.

5.2.2 Performance at Standard Temperature (20°C)

At 20°C, the signal amplitude increases linearly with bias voltage, leading to a monotonic improvement in SNR. Specifically, the rise time shortens to approximately 610 ps, and the estimated jitter ($\sigma_{\text{jitter}} \approx t_{\text{rise}}/\text{SNR}$) decreases to ~ 10 ps at higher voltages.

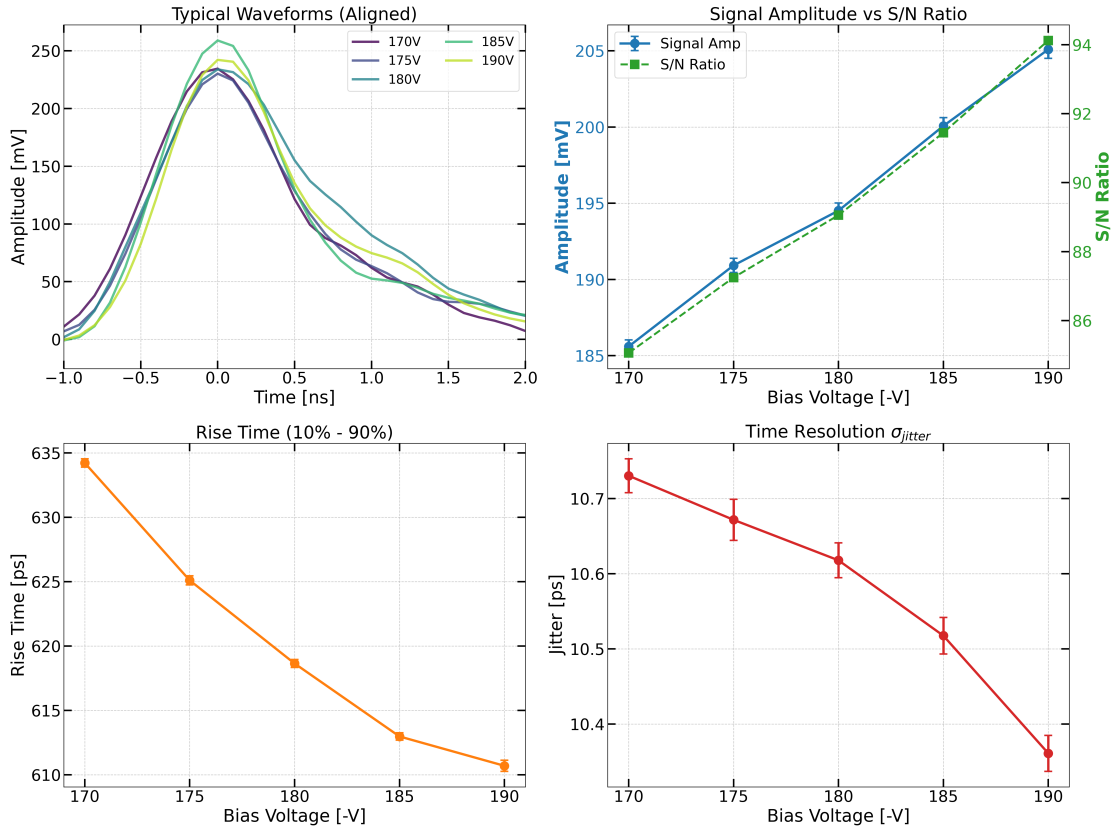

Figure 5.4: Performance dependence on bias voltage at 20°C. (Top-Right) Signal amplitude and SNR, (Bottom-Left) Rise time (10%-90%), (Bottom-Right) Intrinsic jitter estimate. Higher bias voltages improve SNR and reduce rise time.

5.2.3 Determination of Optimal Bias Voltage (V_{opt})

The optimal bias voltage (V_{opt}) was determined to balance high gain with operational stability. A critical factor in this determination is the stability of the effective voltage applied to the sensor, which is given by:

$$V_{\text{eff}} = V_{\text{set}} - I_{\text{leak}} \times R_{\text{protection}} \tag{5.2}$$

where V_{set} is the power supply voltage, I_{leak} is the leakage current, and $R_{\text{protection}} = 1\ \text{M}\Omega$ is the protection resistance in the circuit. Given this resistance, a leakage current of 1 μA results in a voltage drop of 1 V. Such a voltage drop can shift the gain point significantly and degrade the stability of the detector system. Therefore, we established a strict constraint to keep the leakage current within a stable range: $I_{\text{leak}} \leq 1\ \mu\text{A}$.

As shown in the basic characterization, the breakdown voltage (V_{bd}), where the current exceeds this 1 μA threshold, is -190 V at 20°C. Operating exactly at V_{bd}

poses a high risk of instability, as minor temperature fluctuations or voltage ripples could cause the leakage current to violate the constraint and lead to thermal runaway. Consequently, we applied a safety margin of $5 \sim 10$ V from the breakdown point.

Based on these criteria, we selected -185 **V** as the optimal bias voltage for this study.

$$V_{\text{optimal}} = V_{bd} - 5 \text{ V} = -185 \text{ V} \quad (\text{at } 20^{\circ}\text{C}) \tag{5.3}$$

At this voltage, the sensor achieves a high SNR (~ 92) while maintaining a safe margin against breakdown and ensuring the validity of the effective voltage.

5.3 Time Resolution

The time resolution was evaluated using the time difference (Δt) between the AC-LGAD and the MCP-PMT reference detector. To extract the precise timing information, a Constant Fraction Discriminator (CFD) method was applied to the waveforms. The CFD threshold was optimized to 50% for the AC-LGAD and 20% for the reference MCP-PMT to minimize the jitter contribution.

5.3.1 Event Selection and Correction

To evaluate the intrinsic performance of the AC-LGAD, strict event selections and corrections were applied to the dataset:

- **Amplitude Selection:** Events with amplitudes in the high signal-to-noise ratio (S/N) region (> 50 mV) were selected to reduce the timing jitter dominated by electronic noise.
- **Isolation Cut:** AC-LGADs are characterized by signal sharing between adjacent electrodes. Events where the particle hits the inter-pad gap exhibit charge sharing, resulting in lower amplitudes and slower rise times, which degrade the time resolution. To exclude these effects and evaluate the performance at the metal pad center, a strict isolation cut was applied. We required the amplitude of the neighbor channels to be less than 30% of the target channel amplitude ($A_{\text{neighbor}}/A_{\text{target}} < 0.3$).
- **Time-Walk Correction:** The amplitude-dependent time shift (time-walk) was corrected using a profile of Δt as a function of signal amplitude.

5.3.2 Result

Figure 5.5 shows the distribution of Δt fitted with a Gaussian function. The standard deviation (σ_{total}) represents the total system resolution.

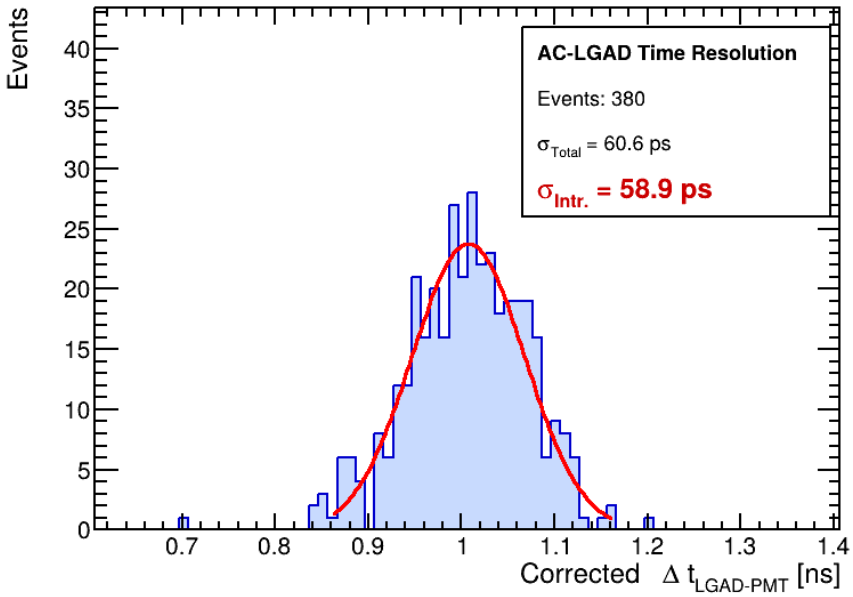

Figure 5.5: Time difference distribution between the AC-LGAD and the MCP-PMT reference. The total time resolution is $\sigma_{total} \approx 59$ ps.

The obtained total time resolution is:

$$\sigma_{\text{total}} \approx 59 \text{ ps} \tag{5.4}$$

To extract the intrinsic performance of the AC-LGAD (σ_{Intr}), we subtract the contributions from the reference detector ($\sigma_{\text{Ref}} \approx 10$ ps) and the electronics jitter ($\sigma_{\text{Jitter}} \approx 10$ ps):

$$\sigma_{\text{Intr}} = \sqrt{\sigma_{\text{total}}^2 - \sigma_{\text{Ref}}^2 - \sigma_{\text{Jitter}}^2} \approx \mathbf{58} \text{ ps} \tag{5.5}$$

The result indicates that the intrinsic resolution is the dominant factor in the current setup ($\sigma_{\text{Intr}} \gg \sigma_{\text{Jitter}}$). The physical factors limiting this resolution, specifically the Landau fluctuations within the sensor bulk, are analyzed in Section 6.1.3.

5.4 Position Reconstruction

The AC-LGAD structure allows for precise position reconstruction through charge sharing between adjacent electrodes. We evaluated the position resolution using the

signal amplitudes induced on the strips.

5.4.1 Center of Gravity Method (Before Correction)

First, the hit position (x_{hit}) was reconstructed using the amplitude-weighted Center of Gravity (CoG) method:

$$x_{hit} = \frac{\sum w_i x_i}{\sum w_i} \tag{5.6}$$

where w_i is the signal amplitude and x_i is the strip position. As shown in Figure 5.6 (Top), the raw CoG distribution exhibits a non-uniform "S-curve" distortion. Events tend to pile up near the strip centers (red regions) and deplete in the inter-strip gaps (green regions). This indicates a non-linear response of the charge sharing mechanism.

5.4.2 Edge Effects

A distinct accumulation of events is observed at the edge channels, Ch1 ($x = 0$ μm) and Ch8 ($x = 3500$ μm). This is an expected edge effect; since there are no readout channels outside these strips, any events originating from the outer regions are reconstructed as having the maximum amplitude at the outermost strip. Therefore, these edge channels accumulate events from a wider effective area than the inner channels. For precise performance evaluation, the inner channels (Ch2 to Ch7), which exhibit a uniform response, are considered valid.

5.4.3 Linearity Improvement via Eta Correction

To correct this non-linearity, we applied the **Eta (η)** Correction method. This method assumes that the incident β-rays illuminate the detector surface uniformly. We defined the relative position variable η and used its Cumulative Distribution Function (CDF) to re-map the coordinates to a uniform distribution:

$$x_{corr} = \text{Pitch} \times (N + \text{CDF}(\eta_{raw})) \tag{5.7}$$

The result of the η correction is shown in Figure 5.6 (Bottom). The dip in the inter-strip regions is eliminated, and a flat, uniform distribution is achieved across the measured channels. This confirms that the local distortions have been removed, allowing the sensor to utilize its full spatial resolution capability.

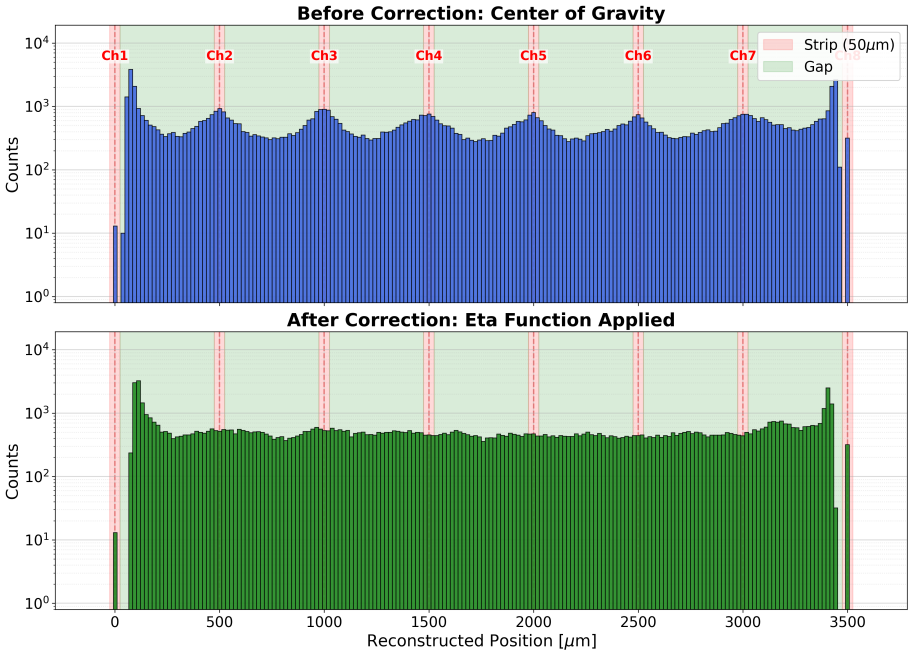

Figure 5.6: (Top) Reconstructed position distribution using the standard Center of Gravity method. A non-linear distortion (pile-up at strip centers) is observed. (Bottom) Distribution after applying Eta (η) correction. The distribution becomes flat across the active area, demonstrating successful linearization.

Chapter 6

Discussion and Outlook

In this chapter, we discuss the physical interpretation of the obtained results, focusing on the temperature dependence of the AC-LGAD characteristics, the factors limiting time resolution, and the linearity of position reconstruction. Finally, we present the outlook for future research, detailing the specific plans for experimental validation and the theoretical connection to EIC physics goals.

6.1 Discussion

6.1.1 Physical Interpretation of I-V Characteristics

The I-V characteristics presented in Chapter 5 exhibited distinct features: a "shoulder" structure indicating depletion, exponential suppression of leakage current, and a significant temperature dependence of the breakdown voltage.

Shoulder Structure at ~ -60 V As shown in Figure 5.1, a slight increase in leakage current is observed around -60 V. Physically, this voltage corresponds to the point where the depletion region extends across the entire gain layer and reaches the bulk region. Beyond this voltage, the observed current is dominated by the generation current from the bulk silicon. This behavior confirms that the sensor is properly depleted and functioning as designed.

Leakage Current Suppression The leakage current in a reverse-biased silicon diode is dominated by the thermal generation of electron-hole pairs in the depletion region (Shockley-Read-Hall generation). The generation current I_{gen} is proportional

to the intrinsic carrier concentration n_i, which depends on temperature T as:

$$I_{\text{gen}} \propto T^2 \exp\left(-\frac{E_g}{2k_B T}\right) \tag{6.1}$$

where E_g is the bandgap energy of silicon and k_B is the Boltzmann constant [20]. Our measurement results show that cooling from +20°C to −10°C reduces the leakage current by an order of magnitude. This exponential suppression is consistent with the theoretical prediction. Lowering the leakage current is crucial not only for reducing the DC power consumption but also for minimizing the shot noise, as discussed in the next subsection.

Temperature Dependence of Breakdown Voltage The breakdown voltage (V_{bd}) shifted towards lower absolute values as the temperature decreased (positive temperature coefficient). This can be explained by the temperature dependence of the charge carrier mean free path. At lower temperatures, lattice vibrations (optical phonons) are suppressed, reducing the probability of carrier scattering. Consequently, carriers can accelerate to the ionization threshold energy more efficiently, triggering the avalanche multiplication at a lower electric field strength. This high sensitivity confirms that for the actual EIC operation, precise temperature control (within ±1°C) or an active bias correction system is mandatory to maintain a stable gain.

6.1.2 Impact of Leakage Current on Signal-to-Noise Ratio

The determination of the optimal bias voltage was heavily influenced by the leakage current behavior. We set a strict threshold of 1 μA, which is justified by two main factors affecting the Signal-to-Noise Ratio (SNR).

First is the **Shot Noise**. The shot noise current (i_n) generated by the detector leakage current (I_{leak}) is given by:

$$i_n = \sqrt{2qI_{\text{leak}}\Delta f} \tag{6.2}$$

where q is the elementary charge and Δf is the bandwidth of the readout system. An increase in leakage current directly raises the noise floor. In our measurements at 40°C or near breakdown, the rapid increase in baseline fluctuations was clearly observed, degrading the SNR.

Second is the **Effective Voltage Drop**. As described in Eq. 5.2, the voltage drop across the protection resistor ($R = 1$ MΩ) reduces the effective bias applied to the gain layer.

$$\Delta V = I_{\text{leak}} \times R \tag{6.3}$$

A leakage current of 1 μA causes a 1 V drop. Since the gain of an LGAD is extremely sensitive to the bias voltage (typically $\Delta M/\Delta V \approx 10$ %/V near breakdown), a fluctuation in leakage current leads to gain instability. Therefore, maintaining the leakage current well below 1 μA via cooling and appropriate voltage selection is essential for stabilizing the detector gain and maximizing the timing resolution.

6.1.3 Limiting Factors of Time Resolution

The intrinsic time resolution was evaluated to be $\sigma_{\text{Intr}} \approx 58$ ps. Using the decomposition $\sigma^2_{\text{AC-LGAD}} = \sigma^2_{\text{Intr}} + \sigma^2_{\text{jitter}} + \sigma^2_{\text{tw}}$, we analyzed the limiting factors.

- **Jitter (σ_{jitter}):** Estimated to be ~ 10 ps due to the high SNR. This is not the dominant factor.
- **Time Walk (σ_{tw}):** Negligible due to the application of the Constant Fraction Discriminator (CFD) method.
- **Landau Fluctuations (σ_{Landau}):** The dominant contribution comes from the intrinsic Landau fluctuations.

Impact of Landau Fluctuations The ^{90}Sr β-source emits electrons with a continuous energy spectrum. When these particles traverse the sensor, electron-hole pairs are generated non-uniformly along the track (Landau distribution). Specifically, the stochastic fluctuations in the depth at which the primary ionization occurs lead to variations in the drift time required for electrons to reach the gain layer. This "Landau jitter" results in an intrinsic timing uncertainty that cannot be corrected by electronics. Our result (~ 58 ps) suggests that the current performance is limited by this physical phenomenon inherent to the sensor thickness (50 μm) and the broad energy spectrum of the source.

6.1.4 Linearity of Position Reconstruction

The position reconstruction analysis highlighted the importance of linearity correction. The raw Center of Gravity (CoG) method resulted in a non-uniform "S-curve" distribution, where reconstructed positions clustered near the strip electrodes. This indicates that the charge sharing ratio is not perfectly linear with respect to the hit position, likely due to the specific impedance of the n^+ resistive layer and signal attenuation.

By applying the **Eta (η) correction**, we successfully linearized the response, achieving a flat event distribution across the strips. This confirms that while the raw signals carry precise position information, a calibration algorithm based on the cumulative distribution function is essential to extract the true impact point and achieve the target spatial resolution of $\mathcal{O}(10)$ μm.

6.2 Outlook

Based on the findings of this thesis, we outline the future roadmap towards the EIC-ePIC experiment, divided into experimental and theoretical approaches.

6.2.1 Experimental Approach: Towards Realistic Conditions

Laser TCT and Test Beams To overcome the limitations of the β-source (broad energy, unknown hit position), we plan to conduct:

- **IR Laser TCT (2026):** To map the precise 2D response function of the sensor and quantify the position-dependent time resolution with μm-level precision.
- **Beam Test at RARiS (March 2026):** To evaluate detection efficiency and tracking performance using high-momentum particles in a telescope setup.

ASIC Integration and Simulation While this study utilized discrete electronics and oscilloscopes for waveform analysis, the final detector will utilize a dedicated Application Specific Integrated Circuit (ASIC), such as the EIC-specific readout chip (e.g., EICROC or HGCROC). To facilitate this transition from analog waveform analysis to high-speed digital readout, we have already initiated the evaluation of the ASIC technology. **As detailed in Appendix A, fundamental characterization of the EICROC0 prototype and functional tests were conducted during the research stay at Brookhaven National Laboratory (BNL).**

Future work will focus on bridging the gap between the sensor and the readout electronics through both experimental and simulation approaches:

- **Hardware Integration (ASIC Readout):** Developing a digital evaluation board that interfaces the AC-LGAD with the ASIC. This will allow for evaluating the sensor performance using the ASIC's discrimination logic and Time-to-Digital Converter (TDC) suitable for the actual EIC-ePIC BTOF detector.
- **Readout Simulation:** Developing a simulation model that integrates the AC-LGAD response with the ASIC's digitization logic.
- **Performance Optimization:** Quantifying the impact of ASIC parameters (e.g., TDC binning, power consumption) on the physics performance.

6.2.2 Theoretical Approach: Physics Sensitivity

The ultimate goal of the BTOF detector is to maximize the physics discovery potential of the EIC. Future studies will focus on connecting the detector performance to physical observables.

- **Proton Mass and Structure:** We aim to evaluate how the improved PID performance contributes to the precise determination of Gravitational Form Factors (GFFs) and the Energy-Momentum Tensor (EMT) of the proton.
- **Impact Study:** We will quantitatively assess the impact of the achieved time resolution (e.g., 35 ps vs 50 ps) on specific reaction channels, such as $ep \to J/\psi p$, to optimize the detector design requirements from a physics perspective.

Through these combined experimental and theoretical efforts, our ultimate goal is the **"Quantification of physics measurement precision based on realistic detector performance"**. This involves calculating the determination precision of Gravitational Form Factors enabled by the improved Particle Identification (PID) capability and evaluating how the detector specifications directly influence the final physics results.

Chapter 7

Conclusion

In this thesis, we have successfully established a comprehensive performance evaluation system for AC-coupled Low Gain Avalanche Detectors (AC-LGADs) at Hiroshima University. This work was motivated by the stringent requirements of the Barrel Time-of-Flight (BTOF) detector for the future Electron-Ion Collider (EIC) ePIC experiment, which demands a timing resolution of approximately 35 ps and precise spatial tracking capabilities.

The constructed experimental setup integrates a ^{90}Sr beta source, a high-precision constant-temperature bath, and a wide-bandwidth readout system utilizing a 2 GHz oscilloscope. This system allows for the detailed characterization of sensor properties under strictly controlled environmental conditions, replicating the operational environment expected in the EIC. Using a prototype strip-type AC-LGAD manufactured by Hamamatsu Photonics K.K. (HPK), we verified the system's performance through a series of systematic measurements.

The key achievements and findings of this study are summarized as follows:

- **Characterization of Temperature Dependence:** We confirmed the significant impact of temperature on the leakage current and breakdown voltage. The results demonstrated that cooling the sensor suppresses the leakage current by an order of magnitude, which is essential for maximizing the signal-to-noise ratio (SNR). Based on the trade-off between gain stability and SNR, we determined the optimal bias voltage to be -185 V at 20°C.
- **Timing Performance:** By employing a Constant Fraction Discriminator (CFD) method and correcting for time-walk effects, we achieved an intrinsic time resolution of approximately **58.9 ps**. While this value includes contributions from the prototype readout electronics, it successfully demonstrates the system's capability to resolve timing on the order of tens of picoseconds using a radioactive source.
- **Verification of Charge Sharing:** We successfully observed the charge

sharing phenomenon between adjacent strips. The continuous reconstruction of hit positions between electrodes confirms that the AC-coupling mechanism functions as designed, promising a spatial resolution significantly superior to the binary resolution of the strip pitch.

In conclusion, the primary objective of this thesis—to construct and validate a robust evaluation system for AC-LGADs—has been fully achieved. The established setup, shown in Figure 7.1, provides a reliable platform for the mass characterization of future sensor prototypes. This work lays the foundation for the upcoming phases of the project, including laser-TCT measurements and beam tests, marking a significant step forward in the development of the ePIC BTOF detector.

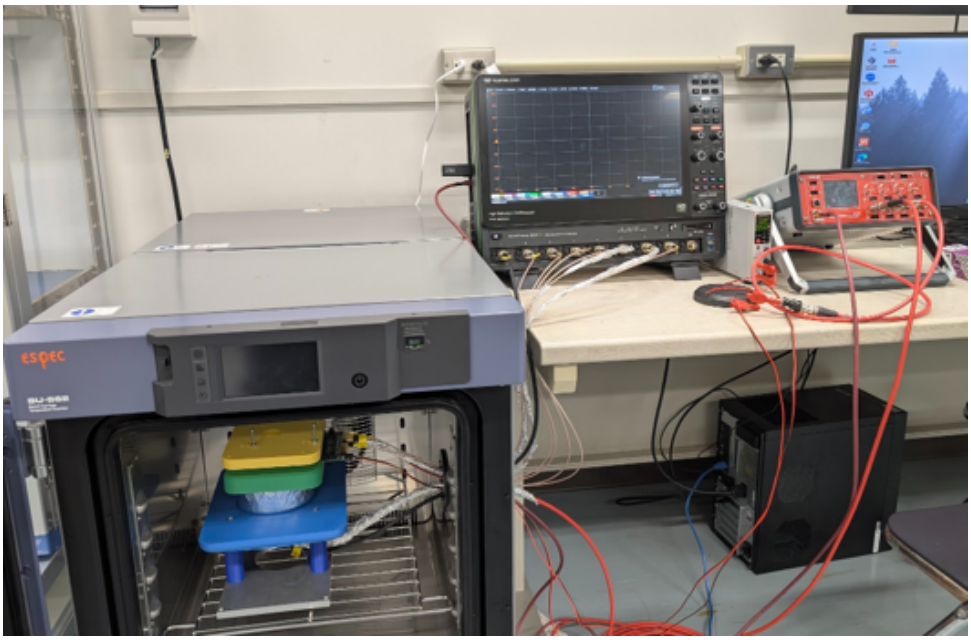

Figure 7.1: The completed AC-LGAD performance evaluation system at Hiroshima University. The setup features a constant-temperature chamber (left) containing the sensor and reference detector, and a high-bandwidth waveform analysis station (right), establishing a ready-to-use environment for EIC sensor development.

Appendix A

Research Activities at BNL

A.1 Overview of the Research Stay

As discussed in Section 6.2.1, the integration of AC-LGAD sensors with dedicated readout electronics is a crucial step for the final detector implementation. To address this technical challenge and gain hands-on experience with the relevant ASIC technology, I conducted research at Brookhaven National Laboratory (BNL) in the United States from September 11, 2024, to February 7, 2025, as part of the U.S.-Japan Science and Technology Cooperation Program in High Energy Physics (Ozaki Exchange Program 2024).

The primary objective of this visit was to evaluate the performance of the readout Application-Specific Integrated Circuit (ASIC) designed for the Time-of-Flight (TOF) detector in the future Electron-Ion Collider (EIC) ePIC experiment. The ePIC TOF system aims to utilize AC-LGAD technology to achieve a time resolution of 30 ps and a spatial resolution of 30 μm. To meet these stringent requirements, the "EICROC0" prototype ASIC has been developed. Under the supervision of Dr. Alessandro Tricoli, I focused on the characterization of the EICROC0 chip and the analysis of the AC-LGAD sensor using a Transient Current Technique (TCT) scan.

A.2 Performance Evaluation of EICROC0 ASIC

A.2.1 EICROC0 Prototype

EICROC0 is a pre-prototype ASIC designed specifically for the readout of pixel-type AC-LGADs. It features a 4×4 readout matrix (16 channels) and is equipped with a transimpedance pre-amplifier, a discriminator, and digital logic to output Time-of-Arrival (TOA) via a Time-to-Digital Converter (TDC) and amplitude information

via an Analog-to-Digital Converter (ADC).

A.2.2 Test Bench Construction

To investigate the response of the ASIC to input charges, I constructed a test bench at BNL. The setup consisted of the EICROC0 test board connected to an FPGA for command execution and data acquisition. Additionally, an oscilloscope was integrated into the system to monitor the analog waveforms output by the pre-amplifier simultaneously with the digital data readout. Figure A.1 shows the constructed test setup.

Figure A.1: The EICROC0 test bench constructed at BNL, consisting of the ASIC test board, an FPGA for control, and a PC for data logging.

A.2.3 Digital Signal Analysis and Results

I played a leading role in the analysis of the digital signals output by the ASIC. A key contribution of this work was the development of analysis code and the identification of the output data structure, which had previously been under-documented.

Linearity and Dynamic Range

We performed charge injection tests by inputting test pulses corresponding to charges ranging from 0.5 fC to 25 fC. Figure A.2 (right) shows the correlation between the injected charge and the mean ADC value. The result demonstrates a clear linearity between the input charge and the digital amplitude output, confirming the proper functioning of the ADC logic for the expected dynamic range.

Timing Resolution (Jitter)

The timing performance was evaluated by analyzing the TDC output. The jitter was calculated as the standard deviation of the TDC distribution (σ_{TDC}). As shown in Figure A.2 (left), the jitter decreases as the signal charge increases. Notably, in the high charge region ($Q > 8$ fC), we achieved a stable time resolution of approximately **13 ps**, which exceeds the required performance of 15–20 ps.

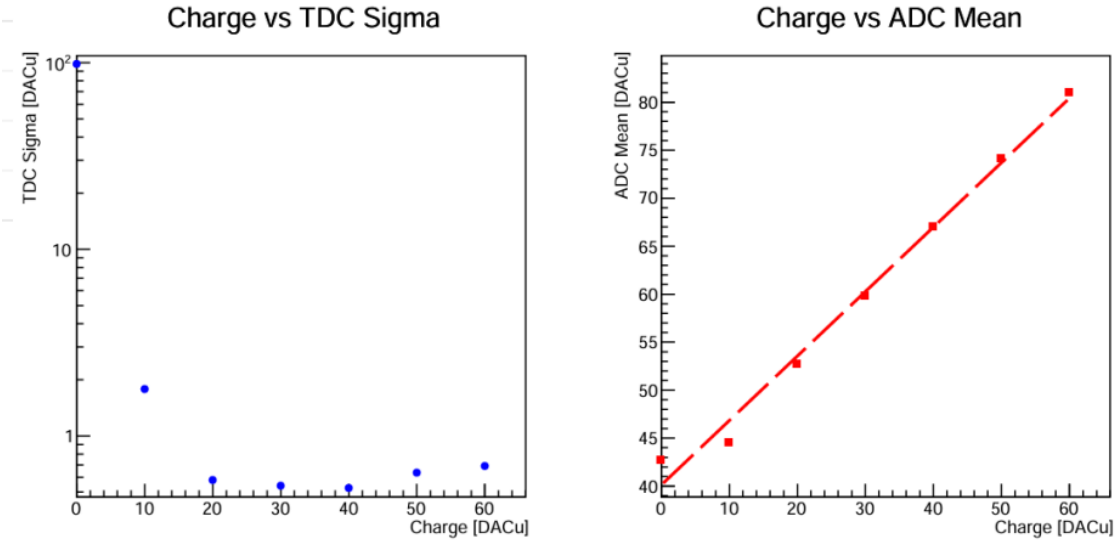

Figure A.2: Evaluation results of the EICROC0 digital readout. (Left) The timing jitter (σ_{TDC}) as a function of injected charge, achieving ∼13 ps at higher charges. (Right) The linearity of the ADC mean value with respect to the input charge.

Channel Uniformity Correction

To ensure uniform operation across all 16 channels, I performed a threshold sweep to characterize the baseline variations. By applying individual threshold corrections (trimming) to each pixel, we successfully suppressed the channel-to-channel response non-uniformity. This process established a method to operate the multi-channel ASIC with a common global threshold.

A.3 TCT Scan Analysis of AC-LGAD

In addition to the ASIC evaluation, I engaged in the characterization of the AC-LGAD sensor using a Transient Current Technique (TCT) system. The TCT scan utilizes a focused laser to induce signals at precise locations on the sensor, allowing for the mapping of the gain uniformity and signal efficiency.

During my stay, I learned the operation of the TCT setup and created a detailed

analysis manual for future users. Although the specific scan performed during this period was affected by wire-bonding defects on the sensor sample, preventing a high-resolution mapping, we were able to confirm the overall gain magnitude and the signal response of the sensor.

A.4 Summary of BNL Activities

Through the activities at BNL, I successfully verified that the EICROC0 prototype ASIC possesses sufficient fundamental performance for the EIC-TOF, particularly regarding linearity and timing resolution ($\sim$13 ps). The digital analysis methods and the test bench established during this stay provide a solid foundation for the future development of the final readout chip.

Appendix B

EIC Physics Overview

This appendix serves as a comprehensive technical supplement to the scientific goals of the Electron-Ion Collider (EIC) introduced in Section 1.3. While the main text outlined the broad motivation for the EIC project, here we delve into the detailed theoretical frameworks and specific experimental observables necessary to address fundamental questions in Quantum Chromodynamics (QCD). We explore four key pillars of the EIC physics program: the origin of the proton mass through the energy-momentum tensor (Section B.1), the resolution of the proton spin puzzle (Section B.2), the multidimensional tomography of the nucleon via GPDs and TMDs (Section B.3), and the exploration of high-density gluon matter and saturation at small Bjorken-x (Section B.4).

B.1 Proton Mass Decomposition and Mechanical Properties

The origin of the proton mass is one of the most fundamental questions in Quantum Chromodynamics (QCD). While the Higgs mechanism accounts for the intrinsic masses of the current quarks, they contribute only about 1% to the total mass of the proton ($\sim$ 938 MeV). The remaining 99% arises from the dynamics of the strong interaction, specifically the energy of quarks and gluons and the quantum trace anomaly. The Electron-Ion Collider (EIC) is expected to play a decisive role in experimentally unraveling this mass budget and exploring the mechanical properties of the nucleon, such as its internal pressure distribution.

B.1.1 Theoretical Framework: Ji Decomposition

The mass of the proton M corresponds to the expectation value of the Hamiltonian density of the QCD energy-momentum tensor (EMT), $T^{\mu\nu}$. According to the gauge-

invariant decomposition proposed by X. Ji [8], the proton mass can be separated into four distinct contributions:

$$M = M_q + E_q + E_g + E_a \tag{B.1}$$

where the terms represent the quark mass contribution (M_q), quark energy (E_q), gluon energy (E_g), and the trace anomaly (E_a). These terms are defined as follows:

$$M_q = \frac{1}{2M} \langle P| \sum_q m_q \bar{\psi}_q \psi_q |P\rangle \,, \tag{B.2}$$

$$E_q = \frac{1}{2M} \langle P| \sum_q \bar{\psi}_q (-i\mathbf{D}\cdot\boldsymbol{\alpha}) \psi_q |P\rangle \,, \tag{B.3}$$

$$E_g = \frac{1}{2M} \langle P| \frac{1}{2}(\mathbf{E}^2 + \mathbf{B}^2) |P\rangle \,, \tag{B.4}$$

$$E_a = \frac{1}{2M} \langle P| \frac{\beta(g)}{2g} G^{\mu\nu} G_{\mu\nu} |P\rangle \,. \tag{B.5}$$

Here, $\langle P|\ldots|P\rangle$ denotes the matrix element in the proton rest frame. E_a is particularly significant as it represents the breaking of scale invariance due to quantum effects, a phenomenon known as the trace anomaly. Recent Lattice QCD calculations by the χQCD Collaboration [30] suggest that at the physical point, the gluon energy and the trace anomaly contribute significantly to the total mass (approximately 36% and 23%, respectively).

B.1.2 Experimental Access via Gravitational Form Factors

Experimentally, the mass distribution and mechanical properties of the proton are encoded in the Gravitational Form Factors (GFFs), which parameterize the matrix elements of the EMT. For a spin-1/2 target, the EMT matrix element is decomposed as:

$$\langle P'|T_g^{\mu\nu}|P\rangle = \bar{u}(P') \left[A_g(t)\gamma^{(\mu}P^{\nu)} + B_g(t)\frac{iP^{(\mu}\sigma^{\nu)\alpha}\Delta_\alpha}{2M} + D_g(t)\frac{\Delta^\mu\Delta^\nu - g^{\mu\nu}\Delta^2}{4M} \right] u(P), \tag{B.6}$$

where $t = (P' - P)^2$ is the squared momentum transfer.

The EIC will access the gluonic GFFs primarily through the near-threshold photoproduction of heavy quarkonium, such as J/ψ ($e + p \to e' + p' + J/\psi$). Theoretical models indicate that the scattering amplitude near the threshold is sensitive to the gluonic scalar form factors and the trace anomaly [31, 32]. By measuring the differential cross-section $d\sigma/dt$ at the EIC with high precision, it will be possible to constrain the gluon mass radius and the trace anomaly contribution [12].

B.1.3 The D-term and Internal Pressure

The form factor $D(t)$, often referred to as the D-term, provides unique insights into the mechanical structure of the proton. It is related to the spatial distribution of the internal forces, specifically the pressure $p(r)$ and shear forces $s(r)$ [33]:

$$T^{ij}(\mathbf{r}) = \left(\frac{r^i r^j}{r^2} - \frac{1}{3}\delta^{ij}\right) s(r) + \delta^{ij} p(r). \tag{B.7}$$

The mechanical stability of the proton requires the von Laue condition to be satisfied: $\int d^3r\, p(r) = 0$. Recent analyses of Deeply Virtual Compton Scattering (DVCS) data have revealed a structure consisting of a repulsive core with extremely high positive pressure near the center and a confining negative pressure at the periphery [34]. The EIC is expected to extend these measurements to the gluon sector, providing a complete picture of the mechanical forces binding the nucleon.

B.2 Proton Spin Decomposition and the Spin Puzzle

The origin of the proton spin (1/2) is another major unresolved problem in hadron physics, often referred to as the "proton spin crisis." In the naive constituent quark model, the proton spin is simply constructed from the spins of its three valence quarks. However, the EMC experiment in the late 1980s revealed that the quark spin contribution $\Delta\Sigma$ is surprisingly small [35], currently determined to be about 30% of the total spin. This implies that the remaining spin budget must be carried by gluons and the orbital angular momentum (OAM) of quarks and gluons. The Electron-Ion Collider is designed to provide the definitive answer to this puzzle.

B.2.1 Theoretical Frameworks: Canonical vs. Kinetic Decompositions

In QCD, the decomposition of the nucleon spin is not unique. Two major gauge-invariant frameworks are widely discussed: the Jaffe-Manohar decomposition and the Ji decomposition.

The **Jaffe-Manohar decomposition** (canonical decomposition) [36] is physically intuitive in the parton model frame (infinite momentum frame). It decomposes the proton spin as:

$$\frac{1}{2} = \frac{1}{2}\Delta\Sigma + \Delta G + L_q^{\text{can}} + L_g^{\text{can}} \tag{B.8}$$

where ΔG is the gluon spin contribution, and L_q^{can} and L_g^{can} are the canonical orbital angular momenta of quarks and gluons, respectively. While ΔG is experimentally

accessible via analyzing powers in polarized proton-proton collisions, the canonical OAM terms are difficult to isolate in gauge-invariant ways experimentally.

The **Ji decomposition** (kinetic decomposition) [37] is based on the gauge-invariant energy-momentum tensor and is given by:

$$\frac{1}{2} = J_q + J_g = \left(\frac{1}{2}\Delta\Sigma + L_q^{\text{Ji}}\right) + J_g \tag{B.9}$$

A key advantage of this framework is that the total angular momenta J_q and J_g can be directly related to Generalized Parton Distributions (GPDs) through the **Ji Sum Rule**:

$$J_{q,g} = \frac{1}{2}\int_{-1}^{1} dx\, x[H_{q,g}(x,\xi,t=0) + E_{q,g}(x,\xi,t=0)]. \tag{B.10}$$

By measuring GPDs H and E in exclusive processes like Deeply Virtual Compton Scattering (DVCS), one can determine J_q and J_g, thereby constraining the kinetic orbital angular momentum L_q^{Ji}.

B.2.2 EIC Physics Goals regarding Spin

Recent global analyses including RHIC data suggest that the gluon spin contribution ΔG is non-zero and positive in the experimentally covered region ($x > 0.05$) [38]. However, large uncertainties remain in the small-x region.

The EIC will address the spin puzzle through two main approaches:

1. **Precision measurement of ΔG:** By measuring the scaling violation of the spin-dependent structure function $g_1(x, Q^2)$ over a wide range of Q^2 and down to low x, the EIC will significantly reduce the uncertainty in the integral of ΔG.

2. **Access to OAM via GPDs:** Through high-luminosity measurements of exclusive processes (DVCS and meson production), the EIC will extract GPDs with high precision. Using the Ji Sum Rule, this will allow for the determination of the orbital angular momentum contribution, which is the last missing piece of the proton spin budget.

B.3 Multidimensional Imaging of the Nucleon: GPDs, TMDs, and Wigner Distributions

While the traditional Parton Distribution Functions (PDFs), $f(x)$, have successfully described the longitudinal momentum structure of the nucleon, they represent only a one-dimensional projection of a complex internal structure. To fully understand

the nucleon's dynamics, including the orbital motion of partons and their spatial distribution, it is necessary to extend this picture to three-dimensional tomography. This is achieved through the frameworks of Generalized Parton Distributions (GPDs) and Transverse Momentum Dependent distributions (TMDs), both of which descend from the fundamental Wigner distributions.

B.3.1 The Wigner Distribution: The Mother Distribution

In quantum mechanics, the Heisenberg uncertainty principle forbids the simultaneous determination of position and momentum. However, in Quantum Chromodynamics (QCD), one can define a phase-space distribution, known as the Wigner distribution $W(x, \mathbf{b}_\perp, \mathbf{k}_\perp)$, which describes the probability of finding a parton with longitudinal momentum fraction x, transverse position $\mathbf{b}_\perp$, and transverse momentum $\mathbf{k}_\perp$ [39].

The Wigner distribution is the most general parton correlator. Integrating out specific degrees of freedom yields the experimentally accessible distributions:

$$\int d^2\mathbf{k}_\perp \, W(x, \mathbf{b}_\perp, \mathbf{k}_\perp) \longrightarrow \text{GPDs (in impact parameter space)} \tag{B.11}$$

$$\int d^2\mathbf{b}_\perp \, W(x, \mathbf{b}_\perp, \mathbf{k}_\perp) \longrightarrow \text{TMDs} \tag{B.12}$$

The EIC aims to reconstruct these distributions to build a comprehensive 5D map of the nucleon.

B.3.2 Generalized Parton Distributions (GPDs)

GPDs provide a unified framework that encompasses both the longitudinal momentum distribution of partons (PDFs) and their spatial distribution (Form Factors). A comprehensive review of the theory, phenomenology, and experimental status of GPDs is given by Diehl [40].

Definitions and Fundamental Properties

At leading twist, there are four chiral-even quark GPDs for the nucleon: $H, E, \tilde{H}$, and $\tilde{E}$. They depend on three kinematic variables: the longitudinal momentum fraction x, the longitudinal momentum transfer (skewness) ξ, and the squared momentum transfer $t = \Delta^2$. According to the rigorous theoretical framework derived from Lorentz invariance and discrete symmetries, GPDs must satisfy the following key constraints [40]:

- **Forward Limit:** In the limit of vanishing momentum transfer ($\xi \to 0, t \to 0$), GPDs reduce to the standard parton distributions. Specifically, H becomes

the unpolarized PDF $q(x)$, and $\tilde{H}$ becomes the polarized PDF $\Delta q(x)$.

$$H^q(x,0,0) = q(x), \quad \tilde{H}^q(x,0,0) = \Delta q(x). \tag{B.13}$$

- **Sum Rules:** The first moments of GPDs are directly related to the elastic form factors of the nucleon (Dirac F_1, Pauli F_2, etc.), independent of ξ. This connects the hard partonic structure to the soft hadronic properties:

$$\int_{-1}^{1} dx H^q(x,\xi,t) = F_1^q(t), \quad \int_{-1}^{1} dx E^q(x,\xi,t) = F_2^q(t). \tag{B.14}$$

- **Polynomiality:** A non-trivial consequence of Lorentz covariance is that the n-th Mellin moment of a GPD must be a polynomial in ξ of degree at most $n+1$. This property is crucial for relating GPD moments to the coefficients of the Energy-Momentum Tensor form factors, linking GPDs to the mechanical properties of the proton (mass, pressure, and shear force) discussed in Section B.1.

Tomography and Spin Structure

One of the most profound implications of GPDs is the concept of **Nucleon Tomography**. The Fourier transform of GPDs with respect to the transverse momentum transfer $\mathbf{\Delta}_\perp$ (at $\xi = 0$) yields the parton distribution in impact parameter space, $q(x, \mathbf{b}_\perp)$ [41]. This provides a probabilistic map of partons in the transverse plane for a given longitudinal momentum x. Furthermore, GPDs provide the only known way to access the parton orbital angular momentum via the **Ji Sum Rule**:

$$J^q = \frac{1}{2} \lim_{t\to 0} \int_{-1}^{1} dx\, x[H^q(x,\xi,t) + E^q(x,\xi,t)]. \tag{B.15}$$

Experimental Access: DVCS and HEMP

While **Deeply Virtual Compton Scattering (DVCS)** ($ep \to ep\gamma$) is the "golden channel" sensitive primarily to H and $\tilde{H}$ through interference with the Bethe-Heitler process, **Hard Exclusive Meson Production (HEMP)** ($ep \to ep\pi/\rho$) offers complementary information. As detailed in Ref. [40], HEMP allows for flavor separation (distinguishing u and d quarks) and provides sensitivity to different GPD combinations; for instance, vector mesons (ρ, ω) probe unpolarized GPDs (H, E), while pseudoscalar mesons (π, η) are sensitive to polarized GPDs $(\tilde{H}, \tilde{E})$. The EIC will utilize both channels to fully disentangle the GPD structure.

B.3.3 Transverse Momentum Dependent Distributions (TMDs)

TMDs, $f(x, \mathbf{k}_\perp)$, describe the three-dimensional motion of partons in momentum space and are essential for understanding the non-perturbative spin-orbit correlations

within the nucleon. A comprehensive overview of the current theoretical and experimental status of TMD physics is provided in the recently published *TMD Handbook* by the OTMD Collaboration [42].

TMD Factorization and Evolution

TMDs are accessed via processes such as **Semi-Inclusive Deep Inelastic Scattering (SIDIS)** ($e + p \to e' + h + X$) and **Drell-Yan** scattering. At small transverse momentum of the produced hadron or lepton pair ($q_T \ll Q$), the cross-section factorizes into a convolution of a TMD PDF and a TMD Fragmentation Function (FF) or another TMD PDF.

Crucially, TMDs depend on the energy scale Q^2 through **TMD evolution equations**, which are governed by the Collins-Soper (CS) kernel. This evolution describes how the transverse momentum distribution broadens as the energy scale increases, connecting measurements at lower energies (e.g., JLab, HERMES) to high-energy colliders (e.g., EIC, RHIC) [42]. The cross-section in the TMD region can be structurally written as:

$$d\sigma \sim \mathcal{H}(Q) \times \int d^2\mathbf{b}_\perp e^{i\mathbf{q}_\perp \cdot \mathbf{b}_\perp} \tilde{f}_q(x, \mathbf{b}_\perp, Q) \tilde{D}_{q\to h}(z, \mathbf{b}_\perp, Q) + \mathcal{O}\left(\frac{q_T}{Q}\right)^2, \qquad \text{(B.16)}$$

where $\mathcal{H}$ is the hard scattering factor, and the soft gluon radiation effects are resumed into the definition of TMDs in b-space.

Key Functions and Universality

Among the various TMDs, two T-odd functions are of particular interest due to their connection to orbital angular momentum and QCD phases:

- **Sivers Function ($f_{1T}^\perp$):** Describes the correlation between the nucleon spin and the parton transverse momentum ($\mathbf{S}_P \cdot (\mathbf{P} \times \mathbf{k}_\perp)$). It arises from the "gauge link" (final state interactions in SIDIS) and is predicted to change sign between SIDIS and Drell-Yan processes (**modified universality**). Verifying this sign change is a major goal of current hadron physics.
- **Collins Function ($H_1^\perp$):** A fragmentation function that couples the transverse spin of a quark to the transverse momentum of the produced hadron. It serves as a chiral-odd partner to measure the quark transversity distribution $h_1(x)$.

B.3.4 The Role of the EIC

The EIC distinguishes itself from existing facilities (such as JLab or COMPASS) through its high center-of-mass energy, high luminosity ($10^{33-34}\,\mathrm{cm}^{-2}\mathrm{s}^{-1}$), and wide

kinematic coverage in x and Q^2.

- For **GPDs**, the EIC's hermetic detectors will ensure the exclusive nature of DVCS events by detecting the recoil proton, allowing for imaging of the gluonic radius and pressure distribution.
- For **TMDs**, the wide kinematic reach allows for the precise study of TMD evolution (how transverse momentum broadens with energy scale), connecting non-perturbative QCD to perturbative regimes.

Ultimately, the EIC aims to unify these observations to construct the Wigner distribution, realizing the full 5D tomography of the proton.

B.4 Physics at Small x: Gluon Saturation

At very high energies (or correspondingly small Bjorken x), the nucleon structure is dominated by gluons. In linear QCD evolution described by the DGLAP or BFKL equations, the gluon density rises rapidly as x decreases due to gluon splitting processes ($g \to gg$). However, this growth cannot continue indefinitely, as it would violate unitarity bounds (Froissart bound). The theory of **Gluon Saturation**, or the **Color Glass Condensate (CGC)**, provides a mechanism to tame this divergence through non-linear gluon recombination ($gg \to g$). The EIC will explore this novel regime of QCD matter, where the gluon density reaches its maximum possible value.

B.4.1 The Saturation Scale and Non-linear Evolution

The onset of saturation is characterized by a dynamical energy scale called the **saturation scale**, $Q_s(x)$. It marks the transition from the dilute parton gas to the dense saturation regime. Phenomenologically, it behaves as:

$$Q_s^2(x) \sim Q_0^2 \left(\frac{1}{x}\right)^{\lambda} A^{1/3}, \tag{B.17}$$

where $\lambda \approx 0.2$–0.3. For momentum transfers $Q^2 < Q_s^2(x)$, the gluon occupancy number becomes large ($n \sim 1/\alpha_s$), and the dynamics are governed by classical strong fields.

The evolution of the gluon density in this non-linear regime is described by the **BK (Balitsky-Kovchegov) equation** [43,44] or the more general **JIMWLK equation**. The BK equation for the scattering amplitude $N(r, Y)$ (where r is the dipole size and $Y = \ln(1/x)$ is the rapidity) reads schematically:

$$\frac{\partial N}{\partial Y} = \bar{\alpha}_s \mathcal{K} \otimes (N - N^2). \tag{B.18}$$

The linear term corresponds to the BFKL evolution (gluon splitting), while the quadratic term $-N^2$ represents the recombination effect, which restores unitarity by enforcing $N \leq 1$ (the black disk limit).

B.4.2 Experimental Signatures at the EIC

While hints of saturation, such as **geometric scaling** [45], were observed at HERA, the EIC will provide definitive evidence through its ability to collide electrons with heavy nuclei ($e + A$). The saturation scale in nuclei is enhanced by a factor of $A^{1/3}$ (the "Oomph factor"), making the saturation regime accessible at moderate x. Key observables include:

1. **Diffractive Cross Sections:** In the saturation regime, the probability of diffractive scattering (where the target remains intact) is predicted to be substantial (up to 20-30% of the total cross-section). The ratio of diffractive to total cross-sections $\sigma_{\text{diff}}/\sigma_{\text{tot}}$ provides a sensitive probe of the saturation dynamics.

2. **Nuclear Shadowing and Structure Functions:** The EIC will precisely measure the nuclear structure function $F_{2A}(x, Q^2)$. The suppression of F_{2A} relative to $A \times F_{2p}$ at small x (shadowing) is a direct consequence of gluon recombination [18, 46].

3. **Di-hadron Correlations:** The saturation momentum Q_s effectively "kicks" partons, leading to a suppression of back-to-back correlations in di-hadron production processes ($e + A \to e' + h_1 + h_2 + X$) at forward rapidities.

Bibliography

[1] Brookhaven National Laboratory. Electron-ion collider. https://www.bnl.gov/eic/. Accessed: 2025-12-09.

[2] E. C. Aschenauer and Rolf Ent. Report on the EIC Project Detector. Presented at the ePIC Collaboration Meeting, BNL (Indico ID 30532), January 2026. Accessed: 2026-01-28. Available at: https://indico.bnl.gov/event/30532/contributions/117971/.

[3] John Lajoie. Status of the ePIC Collaboration. Presented at the ePIC Collaboration Meeting, BNL (Indico ID 30532), January 2026. Accessed: 2026-01-28. Available at: https://indico.bnl.gov/event/30532/contributions/117970/.

[4] Satoshi Yano. Test Article Status: TOF. Presented at the ePIC Collaboration Meeting, BNL (Indico ID 30532), January 2026. Accessed: 2026-01-28. Available at: https://indico.bnl.gov/event/30532/contributions/118883/.

[5] Glenn F. Knoll. *Radiation Detection and Measurement*. John Wiley & Sons, 4th edition, 2010.

[6] David J. Gross and Frank Wilczek. Ultraviolet Behavior of Non-Abelian Gauge Theories. *Phys. Rev. Lett.*, 30:1343–1346, 1973.

[7] H. David Politzer. Reliable Perturbative Results for Strong Interactions? *Phys. Rev. Lett.*, 30:1346–1349, 1973.

[8] Xiang-Dong Ji. A QCD analysis of the mass structure of the nucleon. *Phys. Rev. Lett.*, 74:1071–1074, 1995.

[9] Craig D. Roberts. Perspective on the origin of hadron masses. *Few Body Syst.*, 58(1):5, 2017.

[10] A. Accardi, J. L. Albacete, M. Anselmino, N. Armesto, E. C. Aschenauer, et al. Electron Ion Collider: The Next QCD Frontier: Understanding the glue that binds us all. *Eur. Phys. J. A*, 52(9):268, 2016. [arXiv:1212.1701].

[11] Sergei Nagaitsev. Electron-Ion Collider Design Status. Presented at the ePIC Collaboration Meeting, BNL (Indico ID 30532), January 2026. Accessed: 2026-01-28. Available at: https://indico.bnl.gov/event/30532/contributions/117972/.

[12] R. Abdul Khalek et al. Science requirements and detector concepts for the electron-ion collider: Eic yellow report. *Nuclear Physics A*, 1026:122447, 2022. Comprehensive report on the EIC physics goals and detector requirements (including TOF systems).

[13] D. Kharzeev, H. Satz, A. Syamtomov, and G. Zinovjev. J / psi photoproduction and the gluon structure of the nucleon. *Eur. Phys. J. C*, 9:459–462, 1999.

[14] O. Gryniuk, S. Joosten, Z. E. Meziani, and M. Vanderhaeghen. Upsilon photoproduction on the proton at the Electron-Ion Collider. *Phys. Rev. D*, 102(1):014016, 2020.

[15] Dennis W. Sivers. Single Spin Production Asymmetries from the Hard Scattering of Point-Like Constituents. *Phys. Rev. D*, 41:83, 1990.

[16] John C. Collins. Fragmentation of transversely polarized quarks probed in transverse momentum distributions. *Nucl. Phys. B*, 396:161–182, 1993.

[17] Xiang-Dong Ji. Deeply virtual Compton scattering. *Phys. Rev. D*, 55:7114–7125, 1997.

[18] Larry D. McLerran and Raju Venugopalan. Computing quark and gluon distribution functions for very large nuclei. *Phys. Rev. D*, 49:2233–2241, 1994.

[19] P.A. Zyla et al. Review of Particle Physics. *Prog. Theor. Exp. Phys.*, 2020:083C01, 2020.

[20] S. M. Sze and Kwok K. Ng. *Physics of Semiconductor Devices*. John Wiley & Sons, Hoboken, New Jersey, 3rd edition, 2006. The fundamental reference for semiconductor physics, discussing SRH generation and leakage current mechanisms.

[21] Helmuth Spieler. *Semiconductor Detector Systems*. Oxford University Press, 2005.

[22] S. Ramo. Currents induced by electron motion. *Proceedings of the IRE*, 27(9):584–585, 1939.

[23] G. Pellegrini et al. Technology developments and first measurements of low gain avalanche detectors (lgad) for high energy physics applications. *Nuclear Instruments and Methods in Physics Research Section A: Accelerators, Spectrometers, Detectors and Associated Equipment*, 765:12–16, 2014. The foundational paper describing the concept and first fabrication of LGADs.

[24] C. R. Crowell and S. M. Sze. Temperature dependence of avalanche multiplication in semiconductors. *Applied Physics Letters*, 9(6):242–244, 1966. Discusses the temperature dependence of ionization coefficients and breakdown voltage shift due to phonon scattering.

[25] G. Giacomini et al. Development of the rsd (resistive silicon detector) project. *Nuclear Instruments and Methods in Physics Research Section A: Accelerators, Spectrometers, Detectors and Associated Equipment*, 936:40–41, 2019. Describes the AC-coupled LGAD (RSD) design for precise spatial and temporal resolution.

[26] Koji Nakamura. Development of high time resolution semiconductor tracking detector (ac-lgad). *High Energy News*, 44(1):1, 2025. (in Japanese).

[27] Gabriele Giacomini et al. Development of ac-coupled low gain avalanche diodes. *Nuclear Instruments and Methods in Physics Research Section A*, 934:52–57, 2019.

[28] Japan Radioisotope Association. Strontium-90 (^{90}Sr) beta source. https://www.rcnp.osaka-u.ac.jp/Divisions/rad/document/303ce.pdf. Accessed: 2025-12-09.

[29] PHOTEK. Multi-anode photomultiplier tube. https://www.photek.com/multi-anode/. Accessed: 2026-01-26.

[30] Yi-Bo Yang, Jian Liang, Yu-Jiang Bi, Ying Chen, Terrence Draper, Keh-Fei Liu, and Zhaofeng Liu. Proton Mass Decomposition from the QCD Energy Momentum Tensor. *Phys. Rev. Lett.*, 121(21):212001, 2018.

[31] D. Kharzeev and H. Satz. Quarkonium interactions in QCD. *Phys. Lett. B*, 366:316–322, 1996.

[32] Yoshitaka Hatta and Di-Lun Yang. Holographic J/ψ production near threshold and the proton mass problem. *Phys. Rev. D*, 98(7):074003, 2018.

[33] Maxim V. Polyakov and Peter Schweitzer. Forces inside hadrons: pressure, surface tension, mechanical radius, and all that. *Int. J. Mod. Phys. A*, 33(26):1830025, 2018.

[34] V. D. Burkert, L. Elouadrhiri, and F. X. Girod. The pressure distribution inside the proton. *Nature*, 557(7705):396–399, 2018.

[35] J. Ashman et al. A Measurement of the Spin Asymmetry and Determination of the Structure Function g_1 in Deep Inelastic Muon-Proton Scattering. *Phys. Lett. B*, 206:364, 1988.

[36] R. L. Jaffe and A. Manohar. The G(1) Problem: Fact and Fantasy on the Spin of the Proton. *Nucl. Phys. B*, 337:509–546, 1990.

[37] Xiang-Dong Ji. Gauge-Invariant Decomposition of Nucleon Spin. *Phys. Rev. Lett.*, 78:610–613, 1997.

[38] Daniel de Florian, Rodolfo Sassot, Marco Stratmann, and Werner Vogelsang. Evidence for Polarization of Gluons in the Proton. *Phys. Rev. Lett.*, 113(1):012001, 2014.

[39] A. V. Belitsky, Xiang-Dong Ji, and Feng Yuan. Quark imaging in the proton via quantum phase-space distributions. *Phys. Rev. D*, 69:074014, 2004.

[40] M. Diehl. Generalized parton distributions. *Phys. Rept.*, 388:41–242, 2003.

[41] Matthias Burkardt. Impact parameter dependent parton distributions and off forward parton distributions for zeta $\to$ 0. *Phys. Rev. D*, 62:071503, 2000.

[42] Renaud Boussarie, Matthias Burkardt, Martha Constantinou, William Detmold, Markus Ebert, Michael Engelhardt, Sean Fleming, Leonard Gamberg, Xiangdong Ji, Zhong-Bo Kang, Christopher Lee, Keh-Fei Liu, Simonetta Liuti, Thomas Mehen, Andreas Metz, John Negele, Daniel Pitonyak, Alexei Prokudin, Jian-Wei Qiu, Abha Rajan, Marc Schlegel, Phiala Shanahan, Peter Schweitzer, Iain W. Stewart, Andrey Tarasov, Raju Venugopalan, Ivan Vitev, Feng Yuan, and Yong Zhao. Tmd handbook, 2023.

[43] I. Balitsky. Operator expansion for high-energy scattering. *Nucl. Phys. B*, 463:99–160, 1996.

[44] Yuri V. Kovchegov. Small x F(2) structure function of a nucleus in the perturbative QCD. *Phys. Rev. D*, 60:034008, 1999.

[45] Anna M. Stasto, Krzysztof Golec-Biernat, and J. Kwiecinski. Geometric scaling for the total gamma* p cross-section. *Phys. Rev. Lett.*, 86:596–599, 2001.

[46] L. V. Gribov, E. M. Levin, and M. G. Ryskin. Semihard Processes in QCD. *Phys. Rept.*, 100:1–150, 1983.